Genetically Encoded and Modular SubCellular Organelle Probes (GEM-SCOPe) reveal widespread lysosomal and mitochondrial dysfunction in human *PRKN* knockout astrocytes and neurons

Short title: Fluorescent, live imaging of organelles in human cell models

Camille Goldman[1-5], Tatyana Kareva[1-5], Lily Sarrafha[1-5], Braxton R. Schuldt[1-5], Abhishek Saharsrabudhe[1-3], Tim Ahfeldt[1-5], Joel W. Blanchard[1-5 *]

1. Icahn School of Medicine, Mount Sinai, New York, NY, USA
2. Nash Family Department of Neuroscience, Mount Sinai, New York, NY, USA
3. Friedman Brain Institute, Mount Sinai, New York, NY, USA
4. Ronald M. Loeb Center for Alzheimer's Disease, Mount Sinai, New York, NY USA
5. Black Family Stem Cell Institute, Mount Sinai, New York, NY, USA

* Corresponding author

Email: joel.blanchard@mssm.edu

Abstract

Cellular processes including lysosomal and mitochondrial dysfunction are implicated in the development and progression of many diseases and disorders, including neurodegenerative diseases and cancer. However, there is limited ability to continuously monitor these sub-cellular processes in real-time, and standardized assays to quantify these differences are lacking. Quantitative visualization of mitochondrial and lysosomal networks is crucial to better understand how these organelles are dysregulated during disease pathogenesis. To address this gap, we developed GEM-SCOPe (Genetically Encoded and Modular SubCellular Organelle Probes), an expandable toolbox of genetically encoded fluorescent markers, introduced into cell cultures by lentiviral transduction, which can be used to interrogate changes in proliferation and lysosomal and mitochondrial function in cell models of disease pathogenesis and progression. Genetically encoded fluorescent markers are a powerful tool to consistently visualize subcellular components in live cells without disrupting cellular processes. The fluorophores in GEM-SCOPe are designed to specifically localize to the desired organelle and illuminate information on localization, distribution, organelle turnover, and intracellular oxidative stress. GEM-SCOPe is modular; it can be expanded to include existing or new fluorophores and targeted to other subcellular structures or cell types, increasing the potential for genetically encoded fluorescent markers to probe any cell-model system or subcellular network in live cell cultures. To validate and illustrate the translational functionality of GEM-SCOPe, we applied it to track and quantify sub-cellular pathophysiology changes associated with Parkinson's Disease mediated by loss of function knockout of the *PRKN* gene. We expressed GEM-SCOPe in a *PRKN* knockout induced pluripotent stem cell line, differentiated into astrocytes and neurons, enabling us to track and quantify in real-time disease-associated changes in cellular proliferation, lysosomal distribution, mitochondrial transport and turnover, and reactive oxygen species. Collectively, we demonstrate that GEM-SCOPe is a powerful panel of live-cell fluorescent probes that provide critical insight

39 into the subcellular mechanisms underlying Parkinson's disease in human astrocytes and
40 neurons. GEM-SCOPe can be applied to a diverse range of cellular models of disease to glean
41 an understanding of the underlying mechanisms that promote disease onset and progression.

Abbreviations

BafA1: Bafilomycin A1

COX8A: Cytochrome c Oxidase Subunit 8A

DMSO: Dimethyl Sulfoxide

GEM-SCOPe: Genetically Engineered, Modular, SubCellular Organelle, Probes

H2B: Histone H2B

hiPSC: Human Induced Pluripotent Stem Cell

LAMP1: Lysosomal Associated Membrane Protein 1

PD: Parkinson's Disease

ROS: Reactive Oxygen Species

Introduction

Parkinson's Disease (PD) is a common neurodegenerative disease that robs individuals of their motor and cognitive functions, affecting over 10 million people worldwide and with an estimated 90,000 new diagnoses in the United States each year [1]. PD is clinically characterized by bradykinesia, resting tremor, rigidity, and postural instability [2-5] and pathologically characterized by the loss of dopaminergic neurons in the substantia nigra pars compacta and buildup of intracellular deposits of α-synuclein into insoluble protein aggregates called Lewy Bodies [2, 6-8]. From the first pathological descriptions of PD in the mid-20th century, advancements in many fields, including histology, genetics, cell biology, and neurology enabled insight into many aspects of the disease, from determining genetic and environmental risk factors and mapping disease progression to identifying pathways and proteins to target therapeutically. Despite great progress,

there is still incomplete understanding of the cellular dysfunction that precedes and contributes to chronic neuronal death.

This limited advancement arises in part due to the absence of tools used to track molecular and cellular changes in real-time throughout disease progression. Studies on human post-mortem brain tissue are largely representative of end-stage disease states, making it difficult to dissect which phenotypes are a primary, causative effect and which phenotypes are a secondary response [9]. Mouse models offer more opportunities to study multiple time points throughout disease progression as motor and cognitive symptoms can be monitored over time. However, targeting specific cell types in mice remains technically challenging and time-consuming. Emerging technologies such as the miniscope allow continuous monitoring of fluorescence-based readouts on a cellular level in live mouse and rat brains [10-12]. However, the type of readout from the miniscope has been restricted to neuronal activity from fluorescent calcium sensors and resolution along the z-axis remains a limiting factor in analyzing deeper cortical tissue.

Regardless of such technologies, current genetic rodent models of PD fail to completely recapitulate human disease and lack key pathological hallmarks. Drug-induced models can recapitulate late-stage disease phenotypes and behaviors, but due to their acute onset, are inadequate to study the gradual accumulation of cellular dysfunction that precedes clinical presentation [13, 14]. Advancements in induced pluripotent stem cell (iPSC) differentiation and CRISPR/Cas9 genome editing have led to the emergence of genetic cellular models of PD [15-18]. These models enable researchers to study the effects of genetic and environmental factors on specific human cell populations relevant to PD.

Cellular models of PD provide an exciting opportunity to study subcellular changes and responses to stress or treatment in live cells. Cells can be genetically engineered to express fluorescent proteins that can then be visualized by microscopy in live cells. The applicability of GFP as a reporter gene was immediately appreciated after its identification and isolation in 1962 [19]. Since

89 then, hundreds of fluorophores have been developed by introducing mutations to naturally
90 occurring fluorophores isolated from sea anemones and jellyfish to modulate fluorescence
91 intensity, half-life, and excitation/emission spectra [20]. Additional fluorophores have been
92 developed as biosensors, by fluorescing or changing fluorescence emission in the presence of a
93 certain ligand or under specific cellular conditions [20-25]. Cells can express these fluorophores
94 with virtually limitless possibilities with regards to subcellular localization, cell-type specific
95 expression, and temporally controlled expression. Genetically encoded fluorescent proteins can
96 be used to follow a population of cells as they change due to aging, genetics, or environmental
97 stressors and stimuli.

98 PD has a complex genetic architecture underlying the disease. Over 90% of PD cases are
99 idiopathic; over 90 genetic risk loci have been identified by GWAS, but any of those individual
100 variants confer little risk on their own [26]. The remaining 10% of PD cases can be linked to highly
101 penetrant mutations in a handful of genes. While extremely rare, studying the function of these
102 genes and their impact on cellular processes sheds light on the fundamental pathways that drive
103 PD pathogenesis. Here, we focus on the *PRKN* gene. Autosomal recessive loss of function
104 mutations in *PRKN* are the most frequent known genetic cause of early onset cases of PD,
105 accounting for about 15% of PD cases with onset before the age of 50 [27-30]. *PRKN* encodes
106 for the protein PRKN, an E3 ubiquitin ligase associated with mitochondria. PRKN directs the
107 ubiquitination of outer mitochondrial membrane proteins on damaged mitochondria, targeting
108 them for degradation via the autophagy-lysosomal pathway (mitophagy) [31-33]. While the
109 function of PRKN is well understood, it is still unclear how loss of PRKN function leads to the
110 gradual disease progression of early onset PD. It is believed that neurodegeneration can begin
111 over 20 years before clinical onset, with a prolonged prodromal phase associated with several
112 non-motor symptoms. Thus, it is crucial to study models of early disease to understand what
113 cellular disturbances in the prodromal phase culminate in neurodegeneration.

114 Here, we present GEM-SCOPe (**G**enetically **E**ncoded and **M**odular **S**ub**C**ellular **O**rganelle
115 **P**robes), an expandable panel of genetically encoded reporters to track and quantify the
116 subcellular phenotypes in live cells. We developed a library of constructs that localize specifically
117 to the nucleus, mitochondria, and lysosomes and included fluorophores with a variety of emission
118 spectra or biosensor capabilities. All the lentiviral constructs were developed in the same
119 backbone vector to be modular, enabling any component, be it promotor, localization signal,
120 fluorophore, or antibiotic resistance, to be easily removed or replaced. We validated the
121 fluorophores with live-imaging of human induced pluripotent stem cell (hiPSC)-derived midbrain
122 astrocytes employing existing chemical dyes and chemical perturbations. We then applied GEM-
123 SCOPe to hiPSC-derived astrocytes and neurons from a *PRKN*-knockout model of PD [15]. This
124 revealed previously unseen changes in cellular proliferation, lysosomal distribution, mitochondrial
125 motility and turnover, and reactive oxygen species production. Our results demonstrate the
126 widespread utility of GEM-SCOPe to study a variety of translationally important subcellular
127 changes affected during PD. The modular, combinatorial flexibility of GEM-SCOPe can be
128 adapted to investigate any disease, and, therefore, it is a critical new resource that can be broadly
129 applied in neurodegenerative research and beyond.

130

131 # Results

132 ## Building a modular toolbox for the subcellular localization of
133 genetically encoded fluorophores

134 We developed GEM-SCOPe for live-cell imaging of subcellular organelle dynamics. We aimed to
135 produce a system that is highly modular to easily customize the expression, localization,
136 fluorescence, and selection for any given experimental need. We started with the FUW backbone

137 [41], a 3rd generation lentivirus backbone with a ubiquitin C promoter for high, ubiquitous
138 expression of the transgene across cell types [41, 42] and a woodchuck hepatitis virus post-
139 transcriptional regulatory element (WPRE) for improved lentiviral expression [41, 43, 44]. The
140 designed lentiviral constructs contain four components: promoter, localization sequence,
141 fluorophore, and antibiotic resistance (**Fig. 1A**). The content of these four components can be
142 mixed and matched to generate a library of lentiviral constructs to fit a diverse field of experimental
143 needs. To generate constructs *de novo*, components were combined and inserted into the plasmid
144 via Gibson assembly (**Fig. 1B, top**). Restriction sites were kept between each domain, so each
145 component or group of components could be excised via restriction digest and replaced with a
146 different component, either by restriction site cloning or Gibson assembly (**Fig. 1B, bottom**).
147 Thus, each component of the lentiviral plasmid can be removed or replaced to accommodate
148 features such as cell-type specificity with cell-type specific promoters, alternative subcellular
149 localization, and unique fluorophores.

150 The FUW backbone has a ubiquitin C promoter, but this can be replaced with lineage or cell-type-
151 specific promoters for selective expression in specific cell types or with drug-inducible promoters
152 to temporally control when the construct is transcribed (**Fig. S1A**). Subcellular localization is
153 determined by including the whole or partial coding sequence of a peptide with a known and
154 specific subcellular localization. This domain can be omitted to produce a fluorophore expressed
155 in the cytoplasm. The fluorophore component of the construct offers the most flexibility, from basic
156 fluorescent proteins to more complex fluorophores that change fluorescent excitation and/or
157 emission wavelength with time or environment (**Table S1**).

158 We developed GEM-SCOPe constructs to localize fluorophores to the cytoplasm (no tag), nucleus
159 (H2B-tag), mitochondria (COX8A-tag), and lysosome (LAMP1-tag) (**Fig. 1C**). Fluorophore
160 localization was validated using commercially available live cellular dyes. Nuclear localization was
161 achieved by fusing fluorophores to the C-terminus of histone 2B (H2B). H2B is an integral

162 chromatin protein that is found in all cells and is localized specifically to the nucleus [45, 46]. H2B
163 fused to mTagBFP2, a blue fluorophore, (H2B-mTagBFP2) co-localizes with DRAQ5, a far-red
164 live-cell nuclear dye [47] (**Fig. 1C, top**; Mander's coefficient > 0.99). In addition to the mTagBFP2
165 construct, we also developed lentiviral plasmids with H2B fused to Emerald (green; H2B-Emerald)
166 and mCherry (red; H2B-mCherry) (**Fig. 1A, S1B**).

167 To localize fluorophores to the lysosome, we utilized the N-terminal peptide sequence of
168 lysosomal-associated membrane protein 1 (LAMP1), a major component of lysosomal
169 membranes that plays a key role in lysosomal biogenesis and homeostasis. The N-terminus of
170 LAMP1 fused to mCherry (LAMP1-mCherry) co-localizes with LysoTracker (Thermo Scientific)
171 (**Fig. 1C, middle**; Mander's coefficient = 0.91). LysoTracker is a fluorophore that is partially
172 protonated at neutral pH and can readily cross membranes; once protonated it can no longer
173 diffuse so the fluorescent signal gets trapped in acidic compartments, including, but not limited to,
174 the lysosome [48, 49]. Overexpression of LAMP1 is associated with numerous cancers and
175 cancer metastasis [50-53]. By only using a partial sequence of LAMP1 and not the full peptide
176 sequence, we are able to target the fluorophore specifically to the lysosome without increasing
177 the expression of endogenous LAMP1 (**Fig. S1C**). We also developed lentiviral plasmids with the
178 LAMP1 targeting sequence fused to Emerald (green; LAMP1-Emerald; **Fig. 1A, 1D**).

179 Finally, mitochondrial localization was achieved using the mitochondrial targeting sequence of
180 COX8A. COX8A is a nuclear-encoded subunit of cytochrome-c oxidase (Complex IV) in the
181 electron transport chain [54, 55]. The first 25 amino acid residues of the COX8A peptide sequence
182 target the peptide to the mitochondrial inner membrane and are widely used to specifically localize
183 proteins and fluorophores to the mitochondria [56-58]. To confirm mitochondrial specificity of
184 COX8A-Emerald we compared localization with MitoTracker (Thermo Scientific), a dye that
185 accumulates in the mitochondria due to the negative membrane potential of the inner
186 mitochondrial membrane [48, 59]. The mitochondrial targeting sequence fused to an Emerald

187 fluorophore (COX8A-Emerald) exhibited significant co-localization with MitoTracker (**Fig. 1C,**
188 **bottom**; Mander's coefficient = 0.97). We developed lentiviral plasmids with the COX8A targeting
189 sequence fused to mCherry (red; COX8A-mCherry; **Fig. 1A, 1D**), Timer (green/red; COX8A-
190 Timer; **Fig. 1A, Fig. 5**), and Lemon (cyan/yellow; COX8A-Lemon; **Fig. 1A, Fig. S2**).

191 Once the localization strategies were finalized, we swapped out the fluorophores with different
192 fluorescent proteins that are excited and emitted at alternative wavelengths. Mixing localization
193 sequences and fluorophores with unique emission spectra allows simultaneous imaging of
194 multiple sub-cellular processes in the same cells such as mitochondrial network and lysosomal
195 distribution (**Fig. 1D**). Utilizing a combination of subcellular localization and diverse fluorophores,
196 we developed GEM-SCOPe, a fluorescent, live-cell imaging toolbox of lentiviral constructs that
197 were systematically validated to quantify cellular proliferation, lysosomal distribution, and
198 mitochondrial dynamics in human Parkinson's disease astrocytes.

199

200 H2B-fused fluorophores offer improvements for efficiently
201 labelling nuclei for multi-day live-cell assays

202 Quantification of cellular phenotypes by fluorescence microscopy is dependent on normalization
203 to total cell number. This is often accomplished by counting the number of nuclei. A few fluorescent
204 dyes that can cross the cellular and nuclear membranes of live cells and bind specifically to DNA
205 are commercially available. While efficient for short-term and end-point assays, such dyes
206 intercalate in DNA and therefore have cytotoxic and mutagenic effects [60, 61]. Furthermore,
207 nuclear dyes do not remain contained within the nuclear compartment, and their signal leaches
208 into the cytoplasm in just a few hours after exposing the cells. The cytotoxicity and loss of precise
209 labeling over time render these dyes less useful for long-term microscopy or cell-tracking
210 experiments. To address these concerns, we developed lentiviral constructs expressing nuclear-

211 localized fluorophores by fusing the nucleus-specific histone protein, H2B, with either mTagBFP2,
212 Emerald, or mCherry (**Fig. 1C, 2A**). Human induced pluripotent stem-cell (hiPSC)-derived
213 astrocytes transfected with H2B-mTagBFP2 were co-stained with DRAQ5, a far-red DNA-stain
214 for live cells. The localization of the two nuclear signals was compared 3 hours and 24 hours after
215 the addition of DRAQ5. Immediately after adding DRAQ5, there was no difference between the
216 DRAQ5 stain and the H2B-mTagBFP2 (2-way ANOVA with Tukey's HSD; adj-p = 0.83) (**Fig. 2B,**
217 **C**). Over the experimental period, the DRAQ5 signal spread to where 26% of the DRAQ5 signal
218 was extranuclear (adj-p < 0.0001), while the extranuclear H2B-mTagBFP2 signal did not
219 significantly change (adj-p = 0.99) (**Fig. 2B, C**). While the human eye can still readily distinguish
220 the nucleus from the extranuclear stain in the DRAQ5 images, image analysis programs that rely
221 on grey values for segmentation often fail to correctly differentiate the true nuclear signal from the
222 extranuclear signal. Thus, lentiviral constructs expressing nuclear-localized fluorophores, such as
223 the demonstrated H2B-mTagBFP2, can provide better alternatives for long-term live-imaging
224 experiments with multiple time points.

225

226 H2B-fused fluorophores reveal increased cellular
227 proliferation in PRKN knockout astrocytes

228 While dopaminergic neuron death is the predominant cellular outcome in Parkinson's Disease
229 (PD), other cell types in the brain may change cell cycle regulation under neurotoxic conditions.
230 Tracking cell numbers to monitor proliferation, senescence, or death in vitro can help researchers
231 understand how different cell populations are responding to neurotoxic stress or potential
232 therapeutic strategies.

233 First, we validated that our nuclear-localized construct, H2B-Emerald, could be used to track
234 cellular proliferation. The proliferation of H2B-Emerald transduced hiPSC-derived astrocytes was

235 induced using fetal bovine serum (FBS) or blocked by inhibiting the proteasome with MG-132.
236 Astrocyte proliferation was measured by changes in the number of H2B-Emerald nuclei. As
237 expected, the astrocytes treated with FBS proliferated twice as rapidly as the untreated astrocytes
238 over 48 hours (2-way ANOVA with Tukey's HSD, p-adj = 0.005, **Fig. S3**), while the astrocytes
239 treated with MG-132 did not significantly proliferate over the same period (adj-p = 0.08, **Fig. S3**).
240 Thus, the GEM-SCOPe H2B-fluorophore fusion proteins can be used to track cellular proliferation
241 over multiple days in live cell cultures.

242 To examine the effect of loss of *PRKN* on astrocyte proliferation, we transduced wild-type
243 (*PRKN*$^{+/+}$) astrocytes with H2B-Emerald and isogenic *PRKN* knockout (*PRKN*$^{-/-}$) astrocytes with
244 H2B-mCherry (**Fig. 2D**). Leveraging the modularity of GEM-SCOPe, we were able to mix the two
245 astrocyte populations together and track their proliferation simultaneously. Over 48 hours, the
246 *PRKN*$^{-/-}$ population increased significantly by 25% (2-way ANOVA with Tukey's HSD, p-adj = 0.03;
247 **Fig. 2E, F**) while the *PRKN*$^{+/+}$ population did not proliferate in the same period (2-way ANOVA
248 with Tukey's HSD, p-adj = 0.4; **Fig. 2E, F**). These results contradict mouse studies that found that
249 PRKN-null mice had decreased astroglia proliferation [62]. However, PRKN has also been
250 described as a tumor suppressor, with loss of function mutations arising in a variety of cancers,
251 including glioblastomas [63-65]. Studies on PRKN in the context of cancer find that cancer
252 regulates the degradation of cyclins and cyclin-dependent kinases involved in the G1/S transition,
253 thus promoting continued proliferation [64, 66, 67]. It has been hypothesized that the outcome of
254 loss of function PRKN mutations are highly cell-context dependent; the increased half-life of
255 cyclins leads to cancer in mitotically competent cells while the same cyclins promote apoptosis
256 upon cell cycle reentry in post-mitotic neurons [64, 68-71]. Our findings highlight the importance
257 of studying disease-relevant human cells to capture the intricacies and nuances specific to the
258 human brain that could contribute to PD.

259

LAMP1-localized fluorophores reveal changes in lysosomal distribution in response to chemical and genetic stressors

Lysosomal dysfunction is widely implicated in PD and other forms of neurodegeneration. Several PD-risk and familial genes are involved in the autophagy-lysosomal-endosomal pathway [72-74], and many hallmarks of lysosomal dysfunction associated with familial PD are present in idiopathic PD [73, 75, 76]. Disruption to the autophagy-lysosomal-endosomal pathway is of broad importance in PD and there is a crucial need to study lysosomal function and dysfunction in the context of PD pathogenesis. As described above, we fused the N-terminus of LAMP1 to a fluorophore (Emerald or mCherry) to specifically target the fluorescent signal to the lysosome (**Fig. 1C, 3A**). To validate the GEM-SCOPe LAMP1-mCherry signal responds to lysosomal stress, hiPSC-derived astrocytes transduced with LAMP1-mCherry lentivirus were exposed to bafilomycinA1 (BafA1) for 15 hours. BafA1 inhibits lysosomal proton pump V-ATPases, which blocks autophagosome-lysosome fusion and lysosomal acidification, impairing lysosomal function [77, 78]. hiPSC-derived astrocytes were simultaneously transduced with a non-localized Emerald fluorophore lentivirus, to provide a cell body marker. We used CellProfiler [39] to evaluate the lysosomal number, size, and distribution within each cell. Compared to vehicle (DMSO) treatment, treatment with BafA1 increased the number of LAMP1-mCherry vesicles (unpaired t-test, $p = 0.04$; **Fig. 3B, C**), but did not affect lysosome size (unpaired t-test, $p = 0.16$, **Fig. 3B, C**). Treatment with BafA1 altered the distribution of lysosomes within the astrocytes. Astrocytes treated with BafA1 had a more dispersed distribution of LAMP1-mCherry signal, with only 41% concentrated in the perinuclear area, in contrast to 65% in vehicle-treated astrocytes (unpaired t-test, $p = 0.002$; **Fig. 3B, C**). Perinuclear and juxtanuclear lysosomes have been posited to be more acidic than peripheral lysosomes [79]. Lysosomal distribution can also be affected by cytosolic pH, with acidification promoting the spreading of lysosomes away from the nucleus [80-82]. Since BafA1 inhibits V-ATPases responsible for establishing and maintaining lysosomal pH, the redistribution

285 of lysosomes away from the nucleus upon BafA1 treatment might reflect a change in lysosomal
286 or cytosolic pH, and therefore lysosomal function, in the treated astrocytes.

287 In addition to its role in ubiquitinating damaged mitochondria for degradation via the autophagy-
288 lysosomal pathway [31-33], PRKN has been shown to regulate endosome organization [83] and
289 mitochondria-lysosome contact sites. Although it has been reported that *PRKN* knockout in
290 hiPSC-derived dopaminergic neurons leads to an increase in lysosome number and size
291 compared to isogenic, wild-type dopaminergic neurons [84], the effect of *PRKN* knockout on
292 lysosomes on human astrocytes is largely unknown. Due to PRKN's role in regulating the
293 autophagy-lysosomal pathway, we hypothesized *PRKN*$^{-/-}$ in human astrocytes would disrupt
294 lysosomal dynamics. To test this hypothesis, we applied the same CellProfiler analysis on
295 *PRKN*$^{+/+}$ and *PRKN*$^{-/-}$ hiPSC-derived astrocytes transduced with GEM-SCOPe Emerald and
296 LAMP1-mCherry lentivirus. *PRKN*$^{-/-}$ astrocytes had half as many LAMP1-mCherry vesicles per
297 cell compared to *PRKN*$^{+/+}$ astrocytes (unpaired t-test, $p = 0.003$, **Fig. 3D, E**). Additionally, the
298 *PRKN*$^{-/-}$ lysosomes were smaller than the *PRKN*$^{+/+}$ lysosomes (unpaired t-test, $p = 0.055$, **Fig. 3D,**
299 **E**). Finally, the *PRKN*$^{-/-}$ astrocytes had a decrease in perinuclear LAMP1-mCherry, with only 38%
300 of LAMP1-mCherry signal located in the perinuclear area, compared to 45% in *PRKN*$^{+/+}$ (unpaired
301 t-test, $p = 0.005$, **Fig. 3D, E**). Our results utilizing our GEM-SCOPe LAMP1-mCherry fluorophore
302 suggest that lysosomal distribution in astrocytes is altered upon loss of *PRKN* and further studies
303 to examine lysosomal content and activity are needed to understand the implications and how
304 this could differ from observations in other cell types.

305

306 **Mitochondria-localized fluorophores capture mitochondrial**
307 **fragmentation and alterations in mitochondrial trafficking**
308 **along PRKN knockout dopaminergic neuron axons**

309 Much like lysosomal dysfunction, mitochondrial dysfunction is implicated in PD and
310 neurodegeneration. Therefore, monitoring mitochondrial network dynamics in response to stimuli
311 and stress is important in understanding neurodegenerative diseases. As described above, we
312 fused the N-terminus of the mitochondrial protein COX8A to a fluorophore (Emerald or mCherry)
313 to localize the fluorophore specifically to the mitochondria (**Fig. 1C, 4A**). To validate that GEM-
314 SCOPe COX8A localized fluorophores reflect changes to mitochondrial morphology, we induced
315 mitochondrial stress by treating hiPSC-derived astrocytes transduced with the COX8A-mEmerald
316 lentivirus with 2μM oligomycin for 4 hours. Mitochondrial stress induces fragmentation of the
317 mitochondrial network, which facilitates mitophagy, but also decreases mitochondrial network
318 respiratory capacity [85, 86]. Oligomycin, an inhibitor of ATP synthase, is a known inducer of
319 mitochondrial fragmentation. Treatment with oligomycin induced mitochondrial fragmentation
320 when compared to vehicle-treated astrocytes. The average area of mitochondria was reduced
321 from 1.04 μm^2 in vehicle-treated astrocytes to 0.8 μm^2 in oligomycin-treated astrocytes (1-way
322 ANOVA with Dunett's Test, p-adj = 0.0002; **Fig. 4B, C left)**, and average branch length was
323 reduced from 1.28 μm in vehicle-treated astrocytes to 0.9 μm in oligomycin treated astrocytes (1-
324 way ANOVA with Dunett's Test, p-adj < 0.0001; **Fig. 4B, C middle)**, as expected from a more
325 fragmented mitochondrial network. The aspect ratio is the ratio of the mitochondrial length to
326 width. An aspect ratio of 1 indicates a perfect circle, while larger aspect ratios indicate longer and
327 narrower shapes. The mean aspect ratio decreased from 2.52 in vehicle-treated astrocytes to
328 2.14 in oligomycin-treated astrocytes (1-way ANOVA with Dunett's Test, p-adj < 0.0001; **Fig. 4B,**
329 **C right**), another indicator that mitochondria are fragmenting upon oligomycin treatment. Metrics

330 of mitochondrial network fragmentation (mitochondrial area, branch length, and aspect ratio) are
331 all affected in a dose-dependent manner, with increasing concentrations of oligomycin having
332 increasingly more severe effects on mitochondrial network fragmentation (**Fig. S4**).

333 The transport of mitochondria along neuronal axons is critical for proper synaptic function and
334 neurotransmitter release. We hypothesized *PRKN*$^{-/-}$ may impair axonal mitochondrial transport.
335 To investigate this hypothesis, we transduced wild-type (*PRKN*$^{+/+}$) and *PRKN* knock-out (*PRKN*$^{-/-}$
336) hiPSC-derived midbrain organoids with COX8A-mEmerald. To facilitate imaging of axonal
337 mitochondrial transport, we generated radial axonal arbors by splatting organoids onto the surface
338 of a plate and allowing the axons to grow out [35]. On day 164 of organoid differentiation,
339 fluorescent mitochondria were imaged at high magnification over several minutes to monitor the
340 movement of mitochondria along these axons (**Fig. 4D; Video S1**). In the anterograde direction
341 (moving away from the soma), *PRKN*$^{-/-}$ mitochondria moved only 20% of the distance covered by
342 *PRKN*$^{+/+}$ mitochondria (Welch's t-test, $p < 0.0001$, **Fig. 4E left**) and took 50% longer (unpaired t-
343 test, $p = 0.005$; **Fig. 4E right**). Retrograde-moving mitochondria moved the same distance
344 (unpaired t-test, $p = 0.59$, **Fig. 4F left)** but the *PRKN*$^{-/-}$ mitochondria moved for 150% longer
345 compared to the *PRKN*$^{+/+}$ mitochondria (Welch's t-test, $p = 0.02$; **Fig. 4F right**). PRKN has
346 previously been implicated in mitochondrial transport due to its ubiquitination of mitochondrial
347 motor adaptor complexes [87]. Our results demonstrate that PRKN loss of function impairs
348 mitochondrial trafficking in human neurons, likely reducing the delivery of functional mitochondria
349 synaptic extremities and ultimately compromising neuronal function.

Dynamic fluorophores measure deficiencies in mitochondrial turnover and glutathione reduction potential in PRKN-knockout astrocytes

We demonstrated the utility of single excitation and emission wavelengths to discern phenotypes regarding cellular and subcellular dynamics. Numerous groups have developed fluorophores that change emission wavelengths under certain conditions or circumstances. We introduced several multi-emission fluorophores into GEM-SCOPe to enable quantification of organelle turnover, acidification, and oxidation, in addition to the localization information described with the previous fluorophores.

Fluorescent Timer is a mutated dsRed protein that irreversibly shifts its fluorescence emission from green to red due to tyrosine oxidation and can be used as a molecular clock to track protein turnover (**Fig. 5A**).[22] We, therefore, localized GEM-SCOPe-Timer to the mitochondria (COX8A-Timer), to further investigate mitochondrial turnover [88, 89] (**Fig. 5B**). To first validate COX8A-Timer, mitophagy was inhibited by treating hiPSC-derived astrocytes transduced with COX8A-Timer with the V-ATPase inhibitor bafilomycinA1 (BafA1). BafA1 treatment led to a significant 11% increase in the ratio of red-fluorescent mitochondria over green-fluorescent mitochondria compared to vehicle control astrocytes (unpaired t-test, $p < 0.0001$; **Fig. 5C, D**). Since mitochondrial degradation and turnover occur primarily through mitophagy, inhibition of mitophagy and mitochondrial recycling via BafA1 treatment results in a predicted increase in longer-lived mitochondria.

Because PRKN is directly involved in mitophagy, and we observed impaired retrograde mitochondrial transport in *PRKN*$^{-/-}$ neurons, we wanted to measure changes in mitochondrial turnover in human *PRKN*$^{-/-}$ cells. We transduced wild-type (*PRKN*$^{+/+}$) and *PRKN* knockout *(PRKN*$^{-}$

373 $^{-/-}$) hiPSC-derived astrocytes with GEM-SCOPe COX8A-Timer. The ratio of red-fluorescent signal
374 over green-fluorescent signal increased by 14.5% in *PRKN*$^{-/-}$ astrocytes compared to *PRKN*$^{+/+}$
375 astrocytes (unpaired t-test, p = 0.026, **Fig. 5E, F**). When broken down by individual channel, there
376 was no change in the green fluorescence (2-way ANOVA with Sidak correction, p-adj = 0.1288,
377 **Fig. 5G**), indicating no change in mitochondrial biogenesis. The increase in red to green ratio was
378 driven by a 27% increase in red-fluorescent signal (2-way ANOVA with Sidak correction, p-adj =
379 0.0005, **Fig. 5G**), which is in concordance with an accumulation of older mitochondria due to a
380 failure to properly degrade mitochondria in the absence of PRKN.

381 An expected consequence of impaired mitochondrial recycling is an accumulation of damaged
382 mitochondria and an increase in mitochondria-associated reactive oxygen species (ROS) from
383 inefficient cellular respiration. To measure reactive oxygen levels in live astrocytes, we introduced
384 GRX1-roGFP2, an established fluorophore for measuring ROS, into GEM-SCOPe [25]. GRX1-
385 roGFP2 is a fusion protein between GRX1 and roGFP2. When GRX1 is oxidized by glutathione,
386 it can subsequently oxidize roGFP2. Oxidized roGFP2 shifts its emission spectrum from green
387 fluorescence to blue fluorescence (**Fig. 6A**) [25, 90]. Thus the ratio of green to blue fluorescence
388 is an indicator of glutathione oxidation state. When GRX1-roGFP2 is further coupled with a
389 mitochondrial localization sequence, we can measure the oxidative stress of the mitochondria.

390 This construct was available as a retroviral vector using the signal sequence from *Neurospora*
391 *crassa* ATP synthase protein 9 [25]. When we cloned it into the FUW lentivirus backbone, we
392 decided to keep that localization sequence rather than replace it with the signal sequence for
393 COX8A used in the other GEM-SCOPe mitochondria-localized fluorophores (**Fig. 6B**). To validate
394 GEM-SCOPe GRX1-roGFP2 was working as expected, hiPSC-derived astrocytes transduced
395 with mito-GRX1-roGFP2 were treated with BafA1 to induce oxidative stress [91]. Astrocytes
396 treated with BafA1 had a 30% decrease in the ratio of green fluorescence to blue fluorescence
397 when compared to vehicle (DMSO) treated astrocytes (unpaired t-test, p < 0.0001, **Fig. 6C, D**).

398 The effect is driven by a 40% increase specifically in blue fluorescence (2-way ANOVA with Sidak
399 correction, p-adj < 0.0001, **Fig. 6E**) while the green fluorescence remained unchanged (2-way
400 ANOVA with Sidak correction, p-adj = 0.99, **Fig. 6E**). The increase in blue fluorescence is due to
401 an increase in roGFP2 oxidation, which is indicative of an increase in glutathione oxidation and
402 the presence of reactive oxygen species. Thus, GEM-SCOPe-mito-GRX1-roGFP can be used to
403 monitor glutathione reduction potential and how cells respond to reactive oxygen stress.

404 Because astrocytes play important metabolically supportive roles in the CNS and we observed
405 PRKN-related impairments to mitochondrial recycling with COX8A-Timer (**Fig. 5E-G**), we wanted
406 to understand if PRKN deficiency has effects on ROS production in astrocytes. We transduced
407 *PRKN*$^{+/+}$ and *PRKN*$^{-/-}$ astrocytes with mito-GRX1-roGFP2 lentivirus. Without introducing any
408 additional chemical mitochondrial stressors, we observed an 18% reduction in the ratio of green-
409 fluorescence signal to blue-fluorescence signal in *PRKN*$^{-/-}$ compared to *PRKN*$^{+/+}$ astrocytes
410 (unpaired t-test, p = 0.026; **Fig. 6F, G**). This is indicative of an increase in ROS in *PRKN*$^{-/-}$
411 astrocytes which correlates with our other observation of decreased mitochondrial turnover in the
412 same cells. It has been previously demonstrated that *PRKN*$^{-/-}$ hiPSC-derived dopaminergic
413 neurons show increased cellular ROS [15] and *PRKN*$^{-/-}$ mice have decreased antioxidant
414 capabilities and increased ROS-related protein and lipid damage [92]. By introducing fluorophore-
415 biosensors into our lentiviral catalog, we were able to expand the phenotypes we can observe in
416 live cells to measure changes in the intracellular environment in response to chemical and genetic
417 perturbations.

418

Discussion

Here, we developed and validated GEM-SCOPe (Genetically Engineered, Modular, SubCellular Organelle Probes), a collection of subcellularly targeted fluorophores encoded in a lentiviral backbone. By exploiting the modular design of the constructs, we easily cloned fluorophores with different excitation/emission spectra specified to localize to the nucleus, lysosomes, or mitochondria. We demonstrated that these fluorophores specifically localize to the desired organelle and can quantitatively assess cellular responses to chemical perturbations. Finally, we applied GEM-SCOPe to human *PRKN*-knockout astrocytes and neurons, which revealed widespread perturbations to cellular proliferation, lysosomal distribution, and mitochondrial dynamics, providing new insights into PD pathogenesis.

Gliosis has been widely reported in human post-mortem brain studies of patients with *PRKN* loss-of-function mutations [94-97]. Similar pro-inflammatory phenotypes have also been observed in mouse models and stem-cell-derived glial models of PRKN deficiency [98, 99]. However, there is still a limited understanding of how genetic mutations related to PD modify astrocytes and their role in neurodegeneration. We used GEM-SCOPe to investigate cellular, mitochondrial, and lysosomal dynamics in astrocytes lacking functional PRKN protein. Using nucleus-localized fluorophores, we show that *PRKN* knockout human astrocytes have increased cellular proliferation compared to isogenic, wild-type astrocytes. LAMP1-localized fluorophores revealed that lysosomes in *PRKN* knockout astrocytes are distributed further from the perinuclear nuclear area. Finally, a variety of mitochondria-localized fluorophores revealed that *PRKN* knockout astrocytes have impaired mitochondrial transport, decreased mitochondrial turnover, increased reactive oxygen species, and oxidized glutathione. While additional experiments should be done to support these findings, GEM-SCOPe highlights that there is extensive dysregulation and disruption to normal organelle dynamics in human *PRKN* astrocytes that warrants further investigation.

444 GEM-SCOPe was developed in a 3rd generation lentiviral system. We selected this delivery
445 system because 1) lentiviruses are safe to produce; 2) they infect both dividing and non-dividing
446 cells; and 3) they can be used to develop stable cell lines. 3rd generation lentiviral systems are
447 replication-incompetent, so cells that are transduced with lentivirus cannot produce more viral
448 particles. Only the transfer plasmid, which contains the insert of interest, can be integrated into
449 the host genome; the other plasmids that encode lentiviral structural and envelope genes do not
450 integrate into the host genome, preventing viral replication. Most lentiviruses are produced with
451 VSV-G (Vesicular stomatitis virus G glycoprotein) as the envelope protein, as it provides broad
452 tropism and enables high transduction efficiency in a wide variety of cell types [100]. Finally, GEM-
453 SCOPe lentiviruses were developed with the option to include an antibiotic-resistance gene (**Fig.**
454 **1A**), which can be used to establish stable cell lines that have incorporated the lentiviral load.

455 Although lentiviruses provide a lot of flexibility and safety when delivering genetic information,
456 they also possess some limitations. Lentiviruses have an ideal plasmid size of 9-10kb, and viral
457 titer can decrease if plasmids exceed this size [101]. The H2B-mTagBFP2, H2B-mCherry, and
458 H2B-Emerald lentiviruses (**Fig. 1, 2**) are about 11kb each and transduced hiPSC-derived
459 astrocytes with about 90% efficiency. Coupled with the puromycin resistance that was also
460 included in this construct, we were still able to generate a population with 100% viral transduction
461 despite the size limitation. Another drawback of lentiviral gene delivery is that inserts often
462 integrate into actively transcribed loci [102]. Differentiation of hiPSCs into specific cell types
463 requires extensive chromatin remodeling, and genomic sequences integrated via lentivirus can
464 often be silenced in this process. In the case where hiPSCs must be transduced before
465 differentiation, antibiotic selection during differentiation can select for cells that have integrated
466 the viral load into a genomic region that is not silenced. The final drawback of lentiviral gene
467 delivery is that fluorescence intensity is dependent on the viral copy number in each cell and
468 cannot be used as a readout for organelle abundance. Rather, we need to use measurements

469 like distribution, size, and ratios of different emissions within the same cell. This is not just a
470 limitation of lentiviral gene delivery but of other viral and non-viral delivery systems.

471 In this study, we focused on PD and specifically the alterations to astrocytes with *PRKN* mutations.
472 However, alterations in proliferation, mitochondria, and lysosomes are by no means unique to PD.
473 Many reviews cover the extensive roles of mitochondria and lysosomes in health and disease
474 [103-106]. GEM-SCOPe can be applied beyond neuronal cells and neurodegeneration to
475 countless other cell types to investigate subcellular dynamics that affect disease development
476 and progression. Due to its modular design, GEM-SCOPe can be expanded and molded by
477 research groups to meet specific needs. Different targeting sequences can be integrated to
478 localize fluorophores to relevant subcellular compartments. New fluorophores and biosensors are
479 always being developed to measure additional intracellular conditions. By applying GEM-SCOPe
480 to disease models, we will be able to better understand how cells are disrupted over the course
481 of disease progression, providing insight for future therapeutic targets.

482

483 # Acknowledgements

484 The authors thank Deanna Benson for discussions on mitochondrial transport and kymograph
485 analysis. We thank the Microscopy CoRE at Icahn School of Medicine for providing access to the
486 Leica DMi8 and Thermo Scientific CX7 High Content Screening Platform, as well as training and
487 technical expertise for using these microscopes.

488

Materials and Methods

Molecular cloning

All vectors were derived from pFUW (Addgene plasmid #14882). pFUW was linearized using NheI-HF (NEB R3131) and BamHI-HF (NEB R3136) per manufacturer's protocol, and the desired fragment was gel-purified (Macherey-Nagel 740609). Components of the insert were PCR amplified using Q5-Hot Start DNA Polymerase (NEB M0493) per manufacturer's recommendations. Primers were designed using the NEBuilder Assembly Tool (nebuilder.neb.com) to add 5' and 3' sequences that make the fragments compatible for Gibson assembly and ordered from IDT (Integrated DNA Technologies). Gibson reactions were set up with NEBuilder HiFi DNA Assembly Master Mix (NEB E2621), 50ng of linearized backbone, and 3-fold molar excess of each PCR fragment. For fragments less than 200bp, 5-fold molar excess was used. Reactions were incubated at 50°C for 60 minutes. The Gibson product was transformed in 10-beta competent *E. coli* (NEB C3019) grown on LB Agar plates with 100ug/mL ampicillin. Plasmids from single clones were isolated via miniprep (Macherey-Nagel 740499) and sequenced to confirm successful cloning.

Lentivirus Production

Lentivirus was produced by transfection of HEK293T cells as adapted from Dull et al. 1998 [34]. HEK293T cells were grown in Dulbecco's Modified Eagle Medium (DMEM; Gibco 11965092) with 10% bovine calf serum (Cytiva SH30073) at 37 °C in a 5% CO_2 incubator. The day before transfection, ~10^7 cells were plated per 15cm dish coated in 0.1% gelatin. Media was changed just prior to transfection. For one 15cm dish, 22.5ug of transfer vector was combined with 14.7ug of pMDLg/pRRE (Addgene plasmid #12251), 5.7ug of pRSV.Rev (Addgene plasmid #12253), and

512 7.9ug of pMD2.G (Addgene plasmid #12259) in a 15mL conical tube. The plasmid mixture was
513 added to 1mL of 278 uM $CaCl_2$ (Sigma C1016) and mixed thoroughly before adding 1mL of 2x
514 BBS solution [280 mM NaCl (Fisher Scientific S271-1), 50 mM BES (Millipore 391334), 1.5mM
515 Na_2HPO_4 (Sigma S5136); pH = 6.95] dropwise. Tubes were mixed by inversion, incubated at room
516 temperature for 1 min, and then added dropwise to HEK293T dish. Cell culture media was
517 changed after 16-24 h. Conditioned media was then collected every 24 h for 2 days; conditioned
518 media from the same plate was combined over the two collections. Conditioned media was
519 centrifuged at 2000 x g for 10 minutes to pellet debris and filtered through 0.22-um-pore-size PES
520 filter (Millipore SCGP00525). To concentrate virus, filtered media was incubated with PEG 8000
521 (Sigma P2139) and NaCl, at a final concentration of 5% and 0.15M respectively, overnight at 4°C,
522 then centrifuged at 3000 x g for 20 min. The pellet was resuspended in DMEM/F12 with GlutaMAX
523 (Gibco 10565018) to 1% of the original supernatant volume. The concentrated virus was stored
524 in aliquots at -80°C.

525

526 Midbrain Organoid and Astrocyte Differentiation

527 hiPSC-derived astrocytes were extracted from 100-day-old midbrain organoids as described in
528 Sarrafha et al 2021 and Parfitt et al 2024 [35, 36]. In short, hiPSCs were cultured in StemFlex
529 medium (Gibco A3349401) at 37 °C in a 5% CO_2 incubator. hiPSCs were seeded into 125-mL
530 spinner flasks (Corning 3152) and allowed to self-aggregate in StemFlex (Gibco A3349401)
531 supplemented with 10 μM Y-27632 (Tocris 1254) and 1% Penicillin-Streptomycin (Gibco
532 15140122). Once aggregates were between 300 μm and 500 μm, differentiation was initiated by
533 dual-SMAD inhibition with 10 μM SB431542 (Stemgent 04-0010), 100nM LDN193189 (Tocris
534 6053), 1x B27 without Vitamin A (Gibco 12587010) and 1x N2 (Gibco 17502048) in DMEM-F12
535 with GlutaMAX (Gibco 10565018). Midbrain patterning was achieved with the addition of 3 μM

536 CHIR99021 (Tocris 4423), 2 μM purmorphamine (Stemcell 72204), and 1 μM SAG (Cayman
537 11914) starting 4 days after neural induction. After patterning, media was changed to DMEM/F12
538 with GlutaMAX, supplemented with 1x N2, 1x B27 without Vitamin A, 20 ng/mL GDNF (Peprotech
539 450-10), 20 ng/mL BDNF (Peprotech 450-02), 200 μM L-ascorbic acid (Fisher Scientific BP351),
540 100 μM dibutyryl cAMP (Biogems 1698950), and 10 μM DAPT (Cayman 13197). After 35 days,
541 organoids were transferred to ultra-low attachment plates (Corning 3516), with about 5 organoids
542 per mL of media and cultured in DMEM/F12 with GlutaMAX supplemented with 1x N2, 1x B27
543 without Vitamin A, 10 ng/mL GDNF, 10 ng/mL BDNF, and 200 μM ascorbic acid.

544 Astrocytes were extracted from midbrain organoids starting at day 100. Organoids were gently
545 dissociated in a trypsin enzyme solution (TrypLE Select, Gibco 12563011) using a glass pipette
546 to break up organoids into large chunks. The organoid chunks from 5-10 organoids were placed
547 on 15cm dishes coated with 0.1% gelatin and maintained in Astrocyte Medium (AM; ScienCell
548 #1801). Astrocytes were allowed to grow out of the organoid chunks until the plate was confluent
549 (about 1 week). At this point, astrocytes can be cryopreserved. Astrocytes were maintained in AM
550 and switched to experimental media [1:1 DMEM/F-12:Neurobasal (Gibco 21103049), 1x B27
551 without Vitamin A, 1x N2, 1x MEM-Non-Essential Amino Acids (Gibco 11140050), 1x GlutaMAX
552 (Gibco 35050061), 10 ng/mL CNTF (Peprotech 450-13)] 2-3 days before imaging.

553

554 Astrocyte Viral Transduction

555 iPSC-derived astrocytes were transduced during regular passaging. In short, astrocytes were
556 lifted, spun down, resuspended in AM media, and divided into 1.5mL microcentrifuge tubes,
557 depending on the desired split ratio and number of transductions. The virus was added to the cell
558 suspension and incubated for 5-10 minutes before plating the mixture. Media was topped off such
559 that the final dilution of the virus in media was 1:50. Depending on the viral titer, this dilution

560 sometimes increased or decreased. Astrocytes can also be transduced without passage by
561 adding the virus directly to the media. Media is changed after 24 hours. Antibiotics were added to
562 the media, if relevant, starting at least 3 days after transduction.

563

564 MitoTracker and LysoTracker

565 For MitoTracker staining, astrocytes were incubated with 100 nM of MitoTracker DeepRed
566 (Thermo Scientific M22425) for 30 min at 37 °C. For LysoTracker staining, astrocytes were
567 incubated 100 nM of LysoTracker DeepRed (Thermo Scientific L12492) for 5 min at 37 °C. Cells
568 were then washed twice with PBS before incubation with Hoechst 33342 (Thermo Scientific
569 62249).

570

571 qPCR

572 RNA was extracted from samples using TRIzol (Invitrogen 15596018) and an RNA extraction kit
573 following the manufacturer's recommended protocol (Zymo R2062). RNA concentration and purity
574 were measured on a spectrophotometer. cDNA was produced from 1 ug of RNA per sample, using
575 Maxima H Minus Reverse Transcriptase (Thermo Scientific EP0752) and following the
576 manufacturer's recommendations. qPCR reactions were prepared in a 384-well plate (Applied
577 Biosystems 4309849) with 1:10 dilution of cDNA, 2x PowerUp SYBR Green Master Mix (Applied
578 Biosystems A25741) and 1 μM each of forward and reverse primers. qPCRs were run on
579 QuantStudio 7 (Applied Biosystems 4485701) and analyzed using the ΔΔCt method, normalized
580 to *ACTB*. The following primers were used:

581 *ACTB* Forward: CCTGGCACCCAGCACAAT

582 *ACTB* Reverse: GCCGATCCACACGGAGTA

583 *LAMP1* Forward: CAGATGTGTTAGTGGCACCCA

584 *LAMP1* Reverse: TTGGAAAGGTACGCCTGGATG

585

586 Live Cell Imaging

587 In general, astrocytes were seeded at 10 x 10^3 cells per well of a 96-well plate with a cover glass
588 thickness polystyrene bottom (Greiner 655090) coated in 0.1% gelatin 3-5 days before imaging.
589 Proliferation assays were seeded at 8 x 10^3 cells per well and started 1 day after seeding. Before
590 imaging, cells were incubated with Hoechst 33342 (Thermo Scientific 62249) or DRAQ5 (Thermo
591 Scientific 52251) for 10 minutes.

592 Wide-field live cell imaging was performed using the Thermo Scientific CX7 High Content
593 Screening Platform with 20x and 40x objective lenses (LUCPLFLN20x and LUCPLFLN40x). The
594 microscope was equipped with an incubation unit that maintained temperature, CO_2, and humidity
595 during image acquisition. Confocal images were acquired on a Nikon Ti2E AX R confocal
596 microscope with a 20x objective lens (PLAN APO λD 20x) and 6x optical zoom. Each well was
597 imaged in 5 (confocal) or 25-36 (widefield) different areas, with the average of those images
598 represented as a single data point.

599

600 ImageJ Image Analysis

601 <u>Nuclear Proliferation:</u> Nuclear proliferation was quantified by converting images to a binary based
602 on a threshold and then using 'Analyze Particles' to obtain a count for the number of nuclei in a
603 field. The same threshold and parameters were kept for all time points.

604 Mitochondrial Fragmentation: Mitochondrial fragmentation was measured using the ImageJ
605 plugin, Mitochondrial Analyzer [37]. For thresholding, the “Block Size” was set to 1.45 microns
606 and the “C-Value” was set to 5.

607 Ratiometric Quantification: Ratiometric quantifications for roGFP2, Timer, and Lemon were
608 achieved by measuring the mean grey value in both channels of interest. The values for each
609 channel were then divided to generate the ratio of relative intensity between the two channels.

610 Kymograph Analysis: Kymograph analysis of mitochondrial movement was achieved using the
611 Image J plugins KymographClear 2.0 and KymographDirect [38]. KymographClear 2.0 was used
612 to trace mitochondrial trajectories and generate kymographs from which stationary and motile
613 mitochondria were identified. KymographDirect was then used to extract quantitative information
614 from the trajectories of the motile mitochondria.

615

616 Cell Profiler Image Analysis [39, 40]

617 Subcellular Co-localization: For nuclear co-localization, nuclei in the genetically encoded
618 fluorophore channel and the DRAQ5 channel were identified, and nuclei from cells that were not
619 transduced were filtered out. For lysosomal and mitochondrial co-localization, propagation from
620 the nuclear stain was used to identify cell bodies. Cells were filtered to only analyze those with
621 lentivirus signal within the cell body. Co-localization was reported as the Mander’s coefficient
622 indicating the overlap of the genetically encoded fluorophore with the commercially available
623 stain.

624 Lysosomal Distribution: Cells were defined by nuclei and full cell fluorophore signal. Lamp1-
625 mCherry signal was assigned to the cell body with which it overlapped. Only cells that were
626 successfully transduced were included in the analysis. The distribution of the Lamp1-mCherry

signal was calculated using the “MeasureObjectIntensityDistribution” with two bins generated for each cell using the nuclei as the center of the cell. Bins were scaled such that the inner bin (perinuclear) was always the same percent of total cell area regardless of cell size.

Figure Legends

Fig. 1: A toolbox of lentiviral plasmids developed and validated for subcellular localization of fluorophores (A) Schematic of lentiviral plasmids highlighting the combinatorial power of the toolbox components. Generated using BioRender **(B)** Schematic demonstrating the cloning strategies used to generate the constructs used in this study as well as any future constructs. Generated using BioRender **(C)** Representative images of subcellular localization validation with available dyes in hiPSC-derived astrocytes and Mander’s co-efficient for overlap of the genetically encoded fluorophore with the dye. Top: H2B-mTagBFP2 and DRAQ5 (n = 3; each replicate is an average over 16 images); Middle: LAMP1-mCherry and LysoTracker Deep Red; nuclei stained with Hoechst33342 (n = 4; each replicate is an average over 4 images); Bottom: COX8A-Emerald and MitoTracker Deep Red; nuclei stained with Hoechst33342 (n = 3, each replicate is an average over 36 images). Scale bars = 50 µm **(D)** Representative images of combinatorial applications of GEM-SCOPe. Top: Cell expressing LAMP1-Emerald and COX8A-mCherry. Bottom: cell expression LAMP1-mCherry and COX8A-Emerald. Nuclei were stained with DRAQ5. Scale bars = 50 µm.

Fig. 2: Nucleus-localized fluorophores offer improvements over available stains for multiday imaging (A) Schematic of the lentiviral construct localizing mTagBFP2 to the nucleus with an H2B fusion protein and antibiotic resistance to puromycin used in the following panels **(B)** Representative images of H2B-mTagBFP2 and DRAQ5 nuclear stain 1 hour (top) and 24 hours

650 (bottom) after adding DRAQ5 to the cell cultures. **(C)** Quantification of the percent of stain
651 localized to the nuclear area versus the cytoplasm 1 hour and 24 hours after adding DRAQ5 to
652 cell cultures. (n = 3 per time point; each replicate is an average over 36 images) **(D)** Schematic
653 of the lentiviral construct localizing Emerald or mCherry to the nucleus with an H2B fusion protein
654 and antibiotic resistance to puromycin used in the following panels **(E)** Representative images of
655 nuclei from *PRKN*$^{+/+}$ astrocytes, labeled with H2B-Emerald, and *PRKN* $^{-/-}$ astrocytes, labeled with
656 H2B-mCherry, cultured together during a proliferation assay. Images were taken 24 hours (top)
657 after seeding and 72 hours (bottom) after seeding **(F)** Quantification of number of *PRKN*$^{+/+}$ and
658 *PRKN*$^{-/-}$ nuclei per image field 24 hours and 72 hours after seeding (n = 3 per time point; each
659 replicate is an average over 25 images). Scale bars = 50 µm. All images were acquired on the
660 CX7 HCS platform with a 20x objective lens.

661 **Fig. 3: Lysosome-localized fluorophores reveal changes in lysosomal distribution upon**
662 **chemical and genetic perturbation (A)** Schematic of the lentiviral constructs used in the
663 following panels localizing (top) mCherry to the lysosome with the 5' sequence of *LAMP1* and
664 (bottom) Emerald to the whole cell by not including a localization sequence. **(B)** Representative
665 images of astrocytes transduced with Emerald and LAMP1-mCherry lentiviruses and treated with
666 100 nM bafilomycin A1 (bottom) or a vehicle (DMSO; top). Nuclei were stained with
667 Hoechst33342. Far right: Output from CellProfiler showing the distribution Lamp1-mCherry signal
668 as a fraction of signal in each bin. Darker blue indicates a higher fraction of signal in that bin.
669 Scale bars = 50 µm. **(C)** Quantification of lysosomal number per cell (left), average vesicle area
670 (middle) and fraction of perinuclear lysosomes (right) using Lamp1-mCherry signal in vehicle
671 (DMSO) and bafilomycin A1 (100 nM) treated astrocytes. Emerald was used to determine cell
672 boundaries (n = 4; each replicate is an average over 10 images) **(D)** Representative images of
673 *PRKN*$^{+/+}$ (top) and *PRKN*$^{-/-}$ (bottom) astrocytes transduced with cytoplasmic Emerald and LAMP1-
674 mCherry lentiviruses. Nuclei were stained with Hoechst33342. Far right: Output from CellProfiler

675 showing the distribution Lamp1-mCherry signal as a fraction of signal in each bin. Darker blue
676 indicates a higher fraction of signal in that bin. Scale bars = 25 µm. (**E**) Quantification of Lamp1-
677 mCherry signal in *PRKN*$^{+/+}$ and *PRKN*$^{-/-}$ astrocytes to measure lysosomal number per cell (left),
678 average vesicle area (middle) and fraction of perinuclear lysosomes (right). Emerald fluorescence
679 was used to determine cell boundaries (n = 6; each replicate is an average over 7 images). All
680 images were acquired on a Nikon Ti2E AX R confocal microscope with a 20x objective lens and
681 6x optical zoom.

682 **Fig. 4: Mitochondria-localized fluorophores resolve changes in mitochondrial network**
683 **dynamics (A)** Schematic of the lentiviral construct used in the following panels localizing Emerald
684 to the mitochondria with the targeting sequence of COX8A. **(B)** Representative images of
685 astrocytes transduced with COX8A-Emerald and treated with a vehicle (DMSO; top) or 2 uM
686 oligomycin (bottom). Nuclei were stained with Hoechst33342. High magnification images (far
687 right) highlight the changes to the mitochondrial network upon oligomycin treatment. Scale bars
688 = 50 µm. **(C)** Quantification of mean mitochondrial area, mean mitochondrial branch length, and
689 mean aspect ratio upon oligomycin treatment (n = 3; each replicate is an average over 36 images)
690 **(D)** Representative images of mitochondria labeled with COX8A-Emerald moving along *PRKN*$^{-/-}$
691 neuron axons in the anterograde (left) and retrograde (right) directions. Scale bars = 5 µm. Images
692 were taken on a Leica DMi8 microscope for 1 hour per field **(E-F**). Quantification of mitochondrial
693 run length (left) and run time (right) of COX8A-Emerald labeled mitochondria in *PRKN*$^{+/+}$ and
694 *PRKN*$^{-/-}$ dopaminergic neuron axons moving anterograde (E) and retrograde (F) as determined
695 by kymograph analysis (average of n = 37.5 organoids for anterograde and 23.5 organoids for
696 retrograde; each replicate is an average over 1-3 fields).

697 **Fig. 5: Timer fluorophore measures changes in subcellular mitochondrial turnover in**
698 ***PRKN*$^{-/-}$(A)** Schematic demonstrating how the fluorescent protein Timer works. Timer undergoes
699 a fluorescent shift from a green emission to a red emission overtime; analysis of Timer relies on

700 examining the ratio between the red and green emission. **(B)** Schematic of the lentiviral construct
701 used in the following panels localizing Timer to the mitochondria by using the targeting sequence
702 of COX8A. **(C)** Representative images of astrocytes transduced with COX8A-Timer and treated
703 with a vehicle (DMSO; top) or 100 nM bafilomycin A1 (bottom) for 24 hours. Images were acquired
704 with a 488-excitation line and a 594-excitation line. Far right: ratiometric representation of the red
705 channel divided by the green channel and pseudo colored so that orange, yellow and white
706 indicate more relative red emission and black and purple indicate more relative green emission.
707 Nuclei were stained with DRAQ5. Scale bars = 50 μm. **(D)** Quantification of the ratio of mean
708 intensity of emission from excitation with a 594nm laser to the mean intensity of emission from
709 excitation with a 488 nm laser in astrocytes expressing COX8A-Timer and treated with a vehicle
710 (DMSO) or 100 nM bafilomycin A1 for 24 hours (n = 6; each replicate is an average over 25
711 images). (**E**) Representative images of *PRKN*$^{+/+}$ and *PRKN*$^{-/-}$ astrocytes transduced with COX8A-
712 Timer. Images were acquired with a 488-excitation line and a 594-excitation line. Far right:
713 ratiometric representation of the red channel divided by the green channel and pseudo colored
714 so that orange, yellow and white indicate more relative red emission and black and purple indicate
715 more relative green emission. Nuclei were stained with DRAQ5. Scale bars = 50 μm. **(F)**
716 Quantification of the ratio of mean intensity of emission from excitation with a 594nm laser to the
717 mean intensity of emission from excitation with a 488 nm laser in *PRKN*$^{+/+}$ and *PRKN*$^{-/-}$ astrocytes
718 expressing COX8A-Timer (n = 3; each replicate is an average over 25 images). **(G)** Quantification
719 of mean intensity normalized by nuclear area of green and red fluorescence in *PRKN*$^{+/+}$ and
720 *PRKN*$^{-/-}$ astrocytes expressing COX8A-Timer (n = 3; each replicate is an average over 25 images).
721 All images were acquired on a CX7 HCS platform with a 20x objective lens.

722 **Fig. 6: GRX1-roGFP2 fluorophore is used to quantify glutathione oxidation in chemical and**
723 **genetic models of oxidative stress (A)** Schematic demonstrating how the fluorescent protein
724 fusion Grx1-roGFP2 works. Oxidation of Grx1 upon the oxidation of glutathione results in the

725 eventual oxidation of roGFP2, shifting its emission spectrum from green to blue. **(B)** Schematic
726 of the lentiviral construct used in the following panels localizing Grx1-roGFP2 to the mitochondria.
727 This fluorophore was localized using atp-9 instead of COX8A. **(C)** Representative images of
728 astrocytes transduced with mito-GRX1-roGFP2 and treated with a vehicle (DMSO; top) or 100
729 nM bafilomycin A1 (bottom) for 24 hours. Images were acquired with a 405-excitation laser and a
730 488-excitation laser. Far right: ratiometric representation of the green channel divided by the blue
731 channel and then pseudo colored so that orange, yellow and white indicate more relative green
732 emission while black and purple represent more blue emission. Nuclei were stained with DRAQ5.
733 Scale bars = 50 μm. **(D)** Quantification of the ratio of mean intensity from 488-excitation to the
734 mean intensity from 405 excitation. In astrocytes expression mito-Grx1-roGFP2 and treated with
735 a vehicle or 100 nM bafilomycin A1 (n = 6; each replicate is an average over 25 images). **(E)**
736 Quantification of mean intensity normalized by nuclear area of blue and green fluorescence in
737 vehicle and bafilomycin A1 treated astrocytes expressing mito-Grx1-roGFP2 (n = 6; each replicate
738 is an average of 25 images). **(F)** Representative images of *PRKN*$^{+/+}$ and *PRKN*$^{-/-}$ astrocytes
739 transduced with mito-Grx1-roGFP2. Images were acquired with a 405-excitation laser and a 588-
740 excitation laser. Far right: ratiometric representation of the green channel divided by the blue
741 channel and pseudo colored so that orange, yellow and white indicate more relative green
742 emission and black and purple indicate more relative blue emission. Nuclei were stained with
743 DRAQ5. Scale bars = 50 μm. **(G)** Quantification of the ratio of mean intensity of emission from
744 excitation with a 488nm laser to the mean intensity of emission from excitation with a 405 nm
745 laser in *PRKN*$^{+/+}$ and *PRKN*$^{-/-}$ astrocytes expressing mito-Grx1-roGFP2 (n = 3; each replicate is
746 an average over 16 images).

747

Supporting Information

Fig. S1: GEM-SCOPe supports a diversity of modifications and applications (A) Representative images of astrocytes expressing COX8A-Emerald under the control of a doxycycline inducible promoter. Astrocytes were treated with a vehicle (DMSO; top) or doxycycline (bottom) for 72 hours. Nuclei were stained with Hoechst33342. **(B)** qPCR for endogenous *LAMP1* on RNA from astrocytes transduced with a virus localized to the lysosome (LAMP1-mCherry) or a virus not localized to the lysosome (COX8A-Emerald). qPCR primers were designed to amplify a sequence of *LAMP1* that is not included in the lentivirus to only quantify endogenous *LAMP1* levels. n = 3 independent transductions **(C)** Representative images of a mixed population of astrocytes with nuclei expressing different H2B-fusion fluorophores. Astrocytes were transduced with a single lentivirus and then plated together. Scale bar = 50 μm.

Fig. S2: Mitochondrial pH sensor measures disrupted mitochondrial membrane potential Schematic of the lentiviral construct used in the following panels localizing Lemon, a pH responsive fluorophore, to the mitochondria with the targeting sequence of COX8A. Lemon undergoes Forster Resonance Energy Transfer (FRET) under alkaline conditions. **(B)** Representative images of astrocytes transduced with COX8A-Lemon and treated with a vehicle (DMSO; top) or 2 μM oligomycin (bottom) for 24 hours. Images were acquired with a 455nm-excitation laser and a 515-excitation laser. Far right: ratiometric representation of the emission in the yellow channel divided by the emission in the cyan channel and then pseudo colored so that orange, yellow and white indicate more relative yellow emission (more alkaline) while black and purple represent more cyan emission (more acidic). Nuclei were stained with DRAQ5. Scale bars = 50 μm. **(C)** Quantification of the ratio of yellow emission to cyan emission in astrocytes expressing COX8A-Lemon and treated with DMSO or oligomycin (n = 3; each replicate is an average 36 images).

772 **Fig. S3: Astrocyte proliferation is activated by FBS and inhibited by MG-132 (A)**
773 Representative images of astrocytes transduced with H2B-Emerald lentivirus after 0 hrs (top) or
774 48 hrs (bottom) of treatment with a vehicle (DMSO; left), 10% fetal bovine serum (FBS; middle),
775 or MG132 (right). Scale bars = 50 μm. **(B)** Quantification of number of H2B-Emerald nuclei per
776 image field 0 hours and 48 hours after treatment (n = 6 (n = 3 for MG-132 treatment) per time
777 point; each replicate is an average over 25 images). Scale bars = 50 μm. All images were acquired
778 on the CX7 HCS platform with a 20x objective lens.

779 **Fig. S4: Mitochondrial fragmentation exhibits a dose dependent response to oligomycin-**
780 **induced stress (A)** Representative images of astrocytes transduced with COX8A-Emerald and
781 treated with a vehicle (DMSO), 1μM, 2 μM, or 5 μM oligomycin for 4 hours. Nuclei were stained
782 with Hoechst33342. Scale bars = 50 μm **(B)** Quantification of mitochondrial features indicative of
783 mitochondrial network fragmentation: mean area, perimeter, aspect ratio, number of branches,
784 branch length, and number of branch endpoints (n = 3; each replicate is an average over 36
785 images).

786 **Table S1: GEM-SCOPe lentiviral construct information** A table listing all of the constructs
787 engineered for GEM-SCOPe, including information on AddGene catalog number, localization,
788 fluorophore, and antibiotic selection resistance genes.

789 **Video S1: Mitochondrial axonal transport in *PRKN*$^{+/+}$ and *PRKN*$^{-/-}$ human iPSC derived**
790 **neurons** Representative videos of COX8A-Emerald labeled mitochondria moving within neuronal
791 axons over the course of 1 hour. Images were taken every 10 seconds and sped up 70x. Scale
792 bar = 25 μm.

793

References

1. Willis AW, Roberts E, Beck JC, Fiske B, Ross W, Savica R, et al. Incidence of Parkinson disease in North America. NPJ Parkinsons Dis. 2022;8(1):170.
2. Vazquez-Velez GE, Zoghbi HY. Parkinson's Disease Genetics and Pathophysiology. Annu Rev Neurosci. 2021;44:87-108.
3. Schneider SA, Obeso JA. Clinical and pathological features of Parkinson's disease. Curr Top Behav Neurosci. 2015;22:205-20.
4. Varadi C. Clinical Features of Parkinson's Disease: The Evolution of Critical Symptoms. Biology (Basel). 2020;9(5).
5. Jankovic J. Parkinson's disease: clinical features and diagnosis. J Neurol Neurosurg Psychiatry. 2008;79(4):368-76.
6. Naoi M, Maruyama W. Cell death of dopamine neurons in aging and Parkinson's disease. Mech Ageing Dev. 1999;111(2-3):175-88.
7. Spillantini MG, Schmidt ML, Lee VM, Trojanowski JQ, Jakes R, Goedert M. Alpha-synuclein in Lewy bodies. Nature. 1997;388(6645):839-40.
8. Ohama E, Ikuta F. Parkinson's disease: distribution of Lewy bodies and monoamine neuron system. Acta Neuropathol. 1976;34(4):311-9.
9. Hartmann A. Postmortem studies in Parkinson's disease. Dialogues Clin Neurosci. 2004;6(3):281-93.
10. Helmchen F, Fee MS, Tank DW, Denk W. A miniature head-mounted two-photon microscope. high-resolution brain imaging in freely moving animals. Neuron. 2001;31(6):903-12.
11. Zong W, Wu R, Li M, Hu Y, Li Y, Li J, et al. Fast high-resolution miniature two-photon microscopy for brain imaging in freely behaving mice. Nat Methods. 2017;14(7):713-9.
12. Chen K, Tian Z, Kong L. Advances of optical miniscopes for in vivo imaging of neural activity in freely moving animals. Front Neurosci. 2022;16:994079.
13. Potashkin JA, Blume SR, Runkle NK. Limitations of animal models of Parkinson's disease. Parkinsons Dis. 2010;2011:658083.
14. Chia SJ, Tan EK, Chao YX. Historical Perspective: Models of Parkinson's Disease. Int J Mol Sci. 2020;21(7).
15. Ahfeldt T, Ordureau A, Bell C, Sarrafha L, Sun C, Piccinotti S, et al. Pathogenic Pathways in Early-Onset Autosomal Recessive Parkinson's Disease Discovered Using Isogenic Human Dopaminergic Neurons. Stem Cell Reports. 2020;14(1):75-90.
16. Raja WK, Neves E, Burke C, Jiang X, Xu P, Rhodes KJ, et al. Patient-derived three-dimensional cortical neurospheres to model Parkinson's disease. PLoS One. 2022;17(12):e0277532.
17. Chlebanowska P, Tejchman A, Sulkowski M, Skrzypek K, Majka M. Use of 3D Organoids as a Model to Study Idiopathic Form of Parkinson's Disease. Int J Mol Sci. 2020;21(3).
18. Kim H, Park HJ, Choi H, Chang Y, Park H, Shin J, et al. Modeling G2019S-LRRK2 Sporadic Parkinson's Disease in 3D Midbrain Organoids. Stem Cell Reports. 2019;12(3):518-31.
19. Shimomura O, Johnson FH, Saiga Y. Extraction, purification and properties of aequorin, a bioluminescent protein from the luminous hydromedusan, Aequorea. J Cell Comp Physiol. 1962;59:223-39.
20. Wang M, Da Y, Tian Y. Fluorescent proteins and genetically encoded biosensors. Chem Soc Rev. 2023;52(4):1189-214.
21. Ovechkina VS, Zakian SM, Medvedev SP, Valetdinova KR. Genetically Encoded Fluorescent Biosensors for Biomedical Applications. Biomedicines. 2021;9(11).
22. Terskikh A, Fradkov A, Ermakova G, Zaraisky A, Tan P, Kajava AV, et al. "Fluorescent timer": protein that changes color with time. Science. 2000;290(5496):1585-8.

23. Nakai J, Ohkura M, Imoto K. A high signal-to-noise Ca(2+) probe composed of a single green fluorescent protein. Nat Biotechnol. 2001;19(2):137-41.
24. Burgstaller S, Bischof H, Gensch T, Stryeck S, Gottschalk B, Ramadani-Muja J, et al. pH-Lemon, a Fluorescent Protein-Based pH Reporter for Acidic Compartments. ACS Sens. 2019;4(4):883-91.
25. Gutscher M, Pauleau AL, Marty L, Brach T, Wabnitz GH, Samstag Y, et al. Real-time imaging of the intracellular glutathione redox potential. Nat Methods. 2008;5(6):553-9.
26. Nalls MA, Blauwendraat C, Vallerga CL, Heilbron K, Bandres-Ciga S, Chang D, et al. Identification of novel risk loci, causal insights, and heritable risk for Parkinson's disease: a meta-analysis of genome-wide association studies. Lancet Neurol. 2019;18(12):1091-102.
27. Karimi-Moghadam A, Charsouei S, Bell B, Jabalameli MR. Parkinson Disease from Mendelian Forms to Genetic Susceptibility: New Molecular Insights into the Neurodegeneration Process. Cell Mol Neurobiol. 2018;38(6):1153-78.
28. Jia F, Fellner A, Kumar KR. Monogenic Parkinson's Disease: Genotype, Phenotype, Pathophysiology, and Genetic Testing. Genes (Basel). 2022;13(3).
29. Guadagnolo D, Piane M, Torrisi MR, Pizzuti A, Petrucci S. Genotype-Phenotype Correlations in Monogenic Parkinson Disease: A Review on Clinical and Molecular Findings. Front Neurol. 2021;12:648588.
30. Lesage S, Lunati A, Houot M, Romdhan SB, Clot F, Tesson C, et al. Characterization of Recessive Parkinson Disease in a Large Multicenter Study. Ann Neurol. 2020;88(4):843-50.
31. Pickrell AM, Youle RJ. The roles of PINK1, parkin, and mitochondrial fidelity in Parkinson's disease. Neuron. 2015;85(2):257-73.
32. Tanaka K. The PINK1-Parkin axis: An Overview. Neurosci Res. 2020;159:9-15.
33. Kamienieva I, Duszynski J, Szczepanowska J. Multitasking guardian of mitochondrial quality: Parkin function and Parkinson's disease. Transl Neurodegener. 2021;10(1):5.
34. Dull T, Zufferey R, Kelly M, Mandel RJ, Nguyen M, Trono D, Naldini L. A third-generation lentivirus vector with a conditional packaging system. J Virol. 1998;72(11):8463-71.
35. Sarrafha L, Parfitt GM, Reyes R, Goldman C, Coccia E, Kareva T, Ahfeldt T. High-throughput generation of midbrain dopaminergic neuron organoids from reporter human pluripotent stem cells. STAR Protoc. 2021;2(2):100463.
36. Morrone Parfitt G, Coccia E, Goldman C, Whitney K, Reyes R, Sarrafha L, et al. Disruption of lysosomal proteolysis in astrocytes facilitates midbrain organoid proteostasis failure in an early-onset Parkinson's disease model. Nat Commun. 2024;15(1):447.
37. Chaudhry A, Shi R, Luciani DS. A pipeline for multidimensional confocal analysis of mitochondrial morphology, function, and dynamics in pancreatic beta-cells. Am J Physiol Endocrinol Metab. 2020;318(2):E87-E101.
38. Mangeol P, Prevo B, Peterman EJ. KymographClear and KymographDirect: two tools for the automated quantitative analysis of molecular and cellular dynamics using kymographs. Mol Biol Cell. 2016;27(12):1948-57.
39. Carpenter AE, Jones TR, Lamprecht MR, Clarke C, Kang IH, Friman O, et al. CellProfiler: image analysis software for identifying and quantifying cell phenotypes. Genome Biol. 2006;7(10):R100.
40. Stirling DR, Swain-Bowden MJ, Lucas AM, Carpenter AE, Cimini BA, Goodman A. CellProfiler 4: improvements in speed, utility and usability. BMC Bioinformatics. 2021;22(1):433.
41. Lois C, Hong EJ, Pease S, Brown EJ, Baltimore D. Germline transmission and tissue-specific expression of transgenes delivered by lentiviral vectors. Science. 2002;295(5556):868-72.
42. Schorpp M, Jäger R, Schellander K, Schenkel J, Wagner EF, Weiher H, Angel P. The Human Ubiquitin C Promoter Directs High Ubiquitous Expression of Transgenes in Mice. Nucleic Acids Research. 1996/05/01;24(9).

43. Zufferey R, Donello JE, Trono D, Hope TJ. Woodchuck Hepatitis Virus Posttranscriptional Regulatory Element Enhances Expression of Transgenes Delivered by Retroviral Vectors. Journal of Virology. 1999/04;73(4).
44. Higashimoto T, Urbinati F, Perumbeti A, Jiang G, Zarzuela A, Chang LJ, et al. The woodchuck hepatitis virus post-transcriptional regulatory element reduces readthrough transcription from retroviral vectors. Gene Therapy. 2007;14(17):1298-304.
45. Mosammaparast N, Jackson KR, Guo Y, Brame CJ, Shabanowitz J, Hunt DF, Pemberton LF. Nuclear import of histone H2A and H2B is mediated by a network of karyopherins. J Cell Biol. 2001;153(2):251-62.
46. Marino-Ramirez L, Kann MG, Shoemaker BA, Landsman D. Histone structure and nucleosome stability. Expert Rev Proteomics. 2005;2(5):719-29.
47. Smith PJ, Wiltshire M, Errington RJ. DRAQ5 labeling of nuclear DNA in live and fixed cells. Curr Protoc Cytom. 2004;Chapter 7:Unit 7 25.
48. Zhitomirsky B, Farber H, Assaraf YG. LysoTracker and MitoTracker Red are transport substrates of P-glycoprotein: implications for anticancer drug design evading multidrug resistance. J Cell Mol Med. 2018;22(4):2131-41.
49. Chazotte B. Labeling lysosomes in live cells with LysoTracker. Cold Spring Harb Protoc. 2011;2011(2):pdb prot5571.
50. Dang Q, Zhou H, Qian J, Yang L, Huang J, Zhang Y, Shi W. LAMP1 Overexpression Predicts for Poor Prognosis in Diffuse Large B-cell Lymphoma. Clin Lymphoma Myeloma Leuk. 2018;18(11):749-54.
51. Wang QQ, Yao J, Jin Q, Wang XD, Zhu HJ, Huang F, et al. LAMP1 expression is associated with poor prognosis in breast cancer. Oncol Lett. 2017;14(4):4729-35.
52. Xu Y, Cao X, Zhang S, Zhang Y, Shen Z. High expression of LAMP1 as a prognostic marker in patients with epithelial ovarian cancer. Int J Clin Exp Pathol. 2017;10(8):9104-11.
53. Ranjbar MA, Jamshidi M. Overexpression of Lysosome-Associated Membrane Protein 1 in Oral Squamous Cell Carcinoma and its Correlation with Tumor Differentiation and Metastasis. Iran J Otorhinolaryngol. 2022;34(120):3-8.
54. Zong S, Wu M, Gu J, Liu T, Guo R, Yang M. Structure of the intact 14-subunit human cytochrome c oxidase. Cell Res. 2018;28(10):1026-34.
55. Cunatova K, Reguera DP, Houstek J, Mracek T, Pecina P. Role of cytochrome c oxidase nuclear-encoded subunits in health and disease. Physiol Res. 2020;69(6):947-65.
56. Partikian A, Olveczky B, Swaminathan R, Li Y, Verkman AS. Rapid diffusion of green fluorescent protein in the mitochondrial matrix. J Cell Biol. 1998;140(4):821-9.
57. Hoogewijs K, James AM, Smith RA, Gait MJ, Murphy MP, Lightowlers RN. Assessing the Delivery of Molecules to the Mitochondrial Matrix Using Click Chemistry. Chembiochem. 2016;17(14):1312-6.
58. Candas D, Qin L, Fan M, Li JJ. Experimental Approaches to Study Mitochondrial Localization and Function of a Nuclear Cell Cycle Kinase, Cdk1. J Vis Exp. 2016(108):53417.
59. Chazotte B. Labeling mitochondria with MitoTracker dyes. Cold Spring Harb Protoc. 2011;2011(8):990-2.
60. Durand RE, Olive PL. Cytotoxicity, Mutagenicity and DNA damage by Hoechst 33342. J Histochem Cytochem. 1982;30(2):111-6.
61. Wiezorek C. Cell cycle dependence of Hoechst 33342 dye cytotoxicity on sorted living cells. Histochemistry. 1984;81(5):493-5.
62. Solano RM, Casarejos MJ, Menendez-Cuervo J, Rodriguez-Navarro JA, Garcia de Yebenes J, Mena MA. Glial dysfunction in parkin null mice: effects of aging. J Neurosci. 2008;28(3):598-611.
63. Rouland L, Duplan E, Ramos Dos Santos L, Bernardin A, Katula KS, Manfioletti G, et al. Therapeutic potential of parkin as a tumor suppressor via transcriptional control of cyclins in glioblastoma cell and animal models. Theranostics. 2021;11(20):10047-63.

64. Wahabi K, Perwez A, Rizvi MA. Parkin in Parkinson's Disease and Cancer: a Double-Edged Sword. Mol Neurobiol. 2018;55(8):6788-800.
65. Yeo CW, Ng FS, Chai C, Tan JM, Koh GR, Chong YK, et al. Parkin pathway activation mitigates glioma cell proliferation and predicts patient survival. Cancer Res. 2012;72(10):2543-53.
66. Tay SP, Yeo CW, Chai C, Chua PJ, Tan HM, Ang AX, et al. Parkin enhances the expression of cyclin-dependent kinase 6 and negatively regulates the proliferation of breast cancer cells. J Biol Chem. 2010;285(38):29231-8.
67. Gong Y, Zack TI, Morris LG, Lin K, Hukkelhoven E, Raheja R, et al. Pan-cancer genetic analysis identifies PARK2 as a master regulator of G1/S cyclins. Nat Genet. 2014;46(6):588-94.
68. Veeriah S, Taylor BS, Meng S, Fang F, Yilmaz E, Vivanco I, et al. Somatic mutations of the Parkinson's disease-associated gene PARK2 in glioblastoma and other human malignancies. Nat Genet. 2010;42(1):77-82.
69. Frade JM, Ovejero-Benito MC. Neuronal cell cycle: the neuron itself and its circumstances. Cell Cycle. 2015;14(5):712-20.
70. Kruman, II, Wersto RP, Cardozo-Pelaez F, Smilenov L, Chan SL, Chrest FJ, et al. Cell cycle activation linked to neuronal cell death initiated by DNA damage. Neuron. 2004;41(4):549-61.
71. Gupta R, Jha A, Ambasta RK, Kumar P. Regulatory mechanism of cyclins and cyclin-dependent kinases in post-mitotic neuronal cell division. Life Sci. 2021;285:120006.
72. Gan-Or Z, Dion PA, Rouleau GA. Genetic perspective on the role of the autophagy-lysosome pathway in Parkinson disease. Autophagy. 2015;11(9):1443-57.
73. Navarro-Romero A, Montpeyo M, Martinez-Vicente M. The Emerging Role of the Lysosome in Parkinson's Disease. Cells. 2020;9(11).
74. Hopfner F, Mueller SH, Szymczak S, Junge O, Tittmann L, May S, et al. Rare Variants in Specific Lysosomal Genes Are Associated With Parkinson's Disease. Mov Disord. 2020;35(7):1245-8.
75. Dehay B, Martinez-Vicente M, Caldwell GA, Caldwell KA, Yue Z, Cookson MR, et al. Lysosomal impairment in Parkinson's disease. Mov Disord. 2013;28(6):725-32.
76. Klein AD, Mazzulli JR. Is Parkinson's disease a lysosomal disorder? Brain. 2018;141(8):2255-62.
77. Yoshimori T, Yamamoto A, Moriyama Y, Futai M, Tashiro Y. Bafilomycin A1, a specific inhibitor of vacuolar-type H(+)-ATPase, inhibits acidification and protein degradation in lysosomes of cultured cells. J Biol Chem. 1991;266(26):17707-12.
78. Mauvezin C, Neufeld TP. Bafilomycin A1 disrupts autophagic flux by inhibiting both V-ATPase-dependent acidification and Ca-P60A/SERCA-dependent autophagosome-lysosome fusion. Autophagy. 2015;11(8):1437-8.
79. Johnson DE, Ostrowski P, Jaumouille V, Grinstein S. The position of lysosomes within the cell determines their luminal pH. J Cell Biol. 2016;212(6):677-92.
80. Heuser J. Changes in lysosome shape and distribution correlated with changes in cytoplasmic pH. J Cell Biol. 1989;108(3):855-64.
81. Parton RG, Dotti CG, Bacallao R, Kurtz I, Simons K, Prydz K. pH-induced microtubule-dependent redistribution of late endosomes in neuronal and epithelial cells. J Cell Biol. 1991;113(2):261-74.
82. Pu J, Guardia CM, Keren-Kaplan T, Bonifacino JS. Mechanisms and functions of lysosome positioning. J Cell Sci. 2016;129(23):4329-39.
83. Song P, Trajkovic K, Tsunemi T, Krainc D. Parkin Modulates Endosomal Organization and Function of the Endo-Lysosomal Pathway. J Neurosci. 2016;36(8):2425-37.
84. Okarmus J, Bogetofte H, Schmidt SI, Ryding M, Garcia-Lopez S, Ryan BJ, et al. Lysosomal perturbations in human dopaminergic neurons derived from induced pluripotent stem cells with PARK2 mutation. Sci Rep. 2020;10(1):10278.

995 85. Twig G, Elorza A, Molina AJ, Mohamed H, Wikstrom JD, Walzer G, et al. Fission and
996 selective fusion govern mitochondrial segregation and elimination by autophagy. EMBO J.
997 2008;27(2):433-46.
998 86. Chen H, Chomyn A, Chan DC. Disruption of fusion results in mitochondrial heterogeneity
999 and dysfunction. J Biol Chem. 2005;280(28):26185-92.
1000 87. Wang X, Winter D, Ashrafi G, Schlehe J, Wong YL, Selkoe D, et al. PINK1 and Parkin
1001 target Miro for phosphorylation and degradation to arrest mitochondrial motility. Cell.
1002 2011;147(4):893-906.
1003 88. Hernandez G, Thornton C, Stotland A, Lui D, Sin J, Ramil J, et al. MitoTimer: a novel tool
1004 for monitoring mitochondrial turnover. Autophagy. 2013;9(11):1852-61.
1005 89. Laker RC, Xu P, Ryall KA, Sujkowski A, Kenwood BM, Chain KH, et al. A novel
1006 MitoTimer reporter gene for mitochondrial content, structure, stress, and damage in vivo. J Biol
1007 Chem. 2014;289(17):12005-15.
1008 90. Hanson GT, Aggeler R, Oglesbee D, Cannon M, Capaldi RA, Tsien RY, Remington SJ.
1009 Investigating mitochondrial redox potential with redox-sensitive green fluorescent protein
1010 indicators. J Biol Chem. 2004;279(13):13044-53.
1011 91. Yokomakura A, Hong J, Ohuchi K, Oh SE, Lee JY, Mano N, et al. Increased production
1012 of reactive oxygen species by the vacuolar-type (H(+))-ATPase inhibitors bafilomycin A1 and
1013 concanamycin A in RAW 264 cells. J Toxicol Sci. 2012;37(5):1045-8.
1014 92. Palacino JJ, Sagi D, Goldberg MS, Krauss S, Motz C, Wacker M, et al. Mitochondrial
1015 dysfunction and oxidative damage in parkin-deficient mice. J Biol Chem. 2004;279(18):18614-
1016 22.
1017 93. Kim S, Pajarillo E, Nyarko-Danquah I, Aschner M, Lee E. Role of Astrocytes in
1018 Parkinson's Disease Associated with Genetic Mutations and Neurotoxicants. Cells. 2023;12(4).
1019 94. Cornejo-Olivas MR, Torres L, Mata IF, Mazzetti P, Rivas D, Cosentino C, et al. A
1020 Peruvian family with a novel PARK2 mutation: Clinical and pathological characteristics.
1021 Parkinsonism Relat Disord. 2015;21(5):444-8.
1022 95. Orimo S, Amino T, Yokochi M, Kojo T, Uchihara T, Takahashi A, et al. Preserved cardiac
1023 sympathetic nerve accounts for normal cardiac uptake of MIBG in PARK2. Mov Disord.
1024 2005;20(10):1350-3.
1025 96. Gouider-Khouja N, Larnaout A, Amouri R, Sfar S, Belal S, Ben Hamida C, et al.
1026 Autosomal recessive parkinsonism linked to parkin gene in a Tunisian family. Clinical, genetic
1027 and pathological study. Parkinsonism Relat Disord. 2003;9(5):247-51.
1028 97. Hayashi S, Wakabayashi K, Ishikawa A, Nagai H, Saito M, Maruyama M, et al. An
1029 autopsy case of autosomal-recessive juvenile parkinsonism with a homozygous exon 4 deletion
1030 in the parkin gene. Mov Disord. 2000;15(5):884-8.
1031 98. Schmidt S, Linnartz B, Mendritzki S, Sczepan T, Lubbert M, Stichel CC, Lubbert H.
1032 Genetic mouse models for Parkinson's disease display severe pathology in glial cell
1033 mitochondria. Hum Mol Genet. 2011;20(6):1197-211.
1034 99. Gerasimova T, Stepanenko E, Novosadova L, Arsenyeva E, Shimchenko D, Tarantul V,
1035 et al. Glial Cultures Differentiated from iPSCs of Patients with PARK2-Associated Parkinson's
1036 Disease Demonstrate a Pro-Inflammatory Shift and Reduced Response to TNFalpha
1037 Stimulation. Int J Mol Sci. 2023;24(3).
1038 100. Hastie E, Cataldi M, Marriott I, Grdzelishvili VZ. Understanding and altering cell tropism
1039 of vesicular stomatitis virus. Virus Res. 2013;176(1-2):16-32.
1040 101. Sweeney NP, Vink CA. The impact of lentiviral vector genome size and producer cell
1041 genomic to gag-pol mRNA ratios on packaging efficiency and titre. Mol Ther Methods Clin Dev.
1042 2021;21:574-84.
1043 102. Desfarges S, Ciuffi A. Retroviral integration site selection. Viruses. 2010;2(1):111-30.
1044 103. Bonam SR, Wang F, Muller S. Lysosomes as a therapeutic target. Nat Rev Drug Discov.
1045 2019;18(12):923-48.

1046 104. Zhang Z, Yue P, Lu T, Wang Y, Wei Y, Wei X. Role of lysosomes in physiological
1047 activities, diseases, and therapy. J Hematol Oncol. 2021;14(1):79.
1048 105. Javadov S, Kozlov AV, Camara AKS. Mitochondria in Health and Diseases. Cells.
1049 2020;9(5).
1050 106. Chen W, Zhao H, Li Y. Mitochondrial dynamics in health and disease: mechanisms and
1051 potential targets. Signal Transduct Target Ther. 2023;8(1):333.

1052

Figure 1

A.

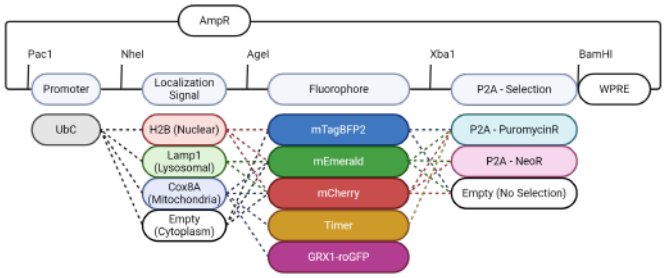

B.

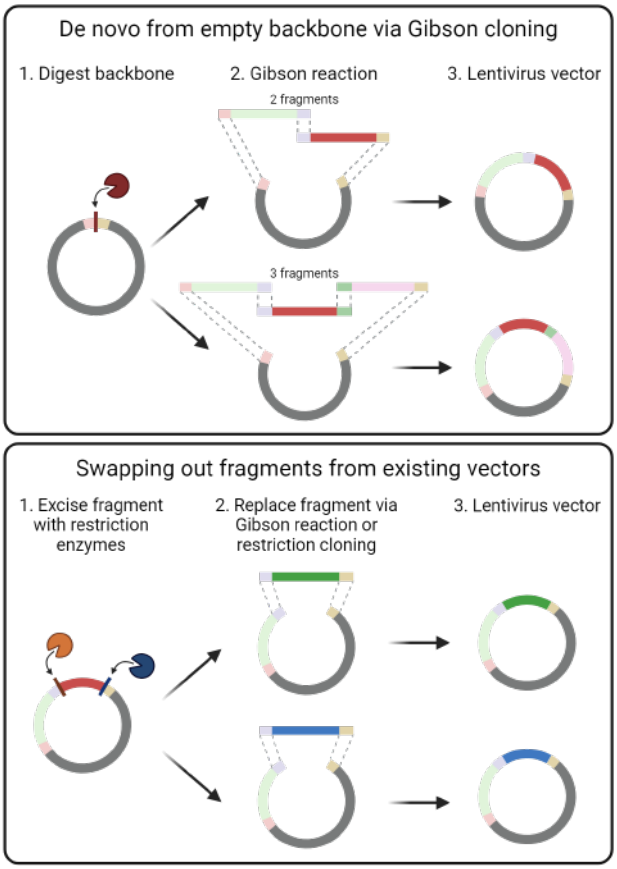

C.

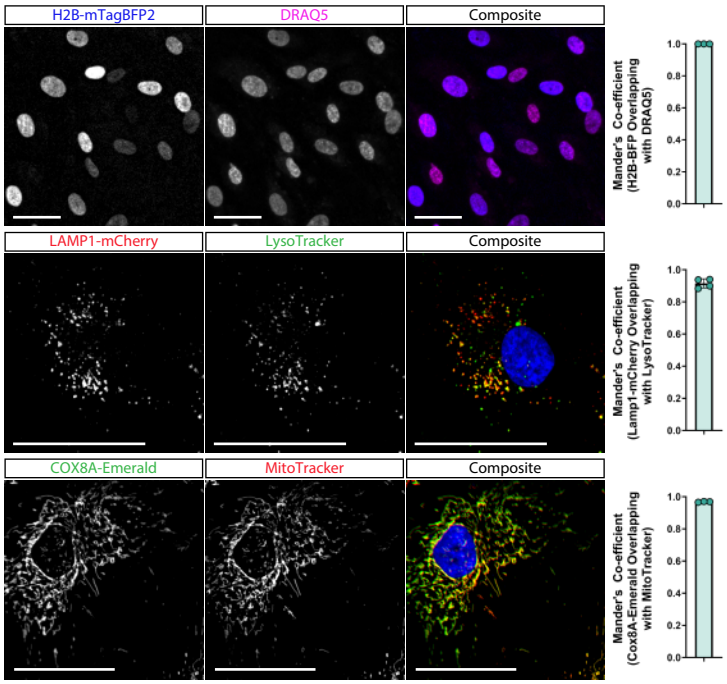

D.

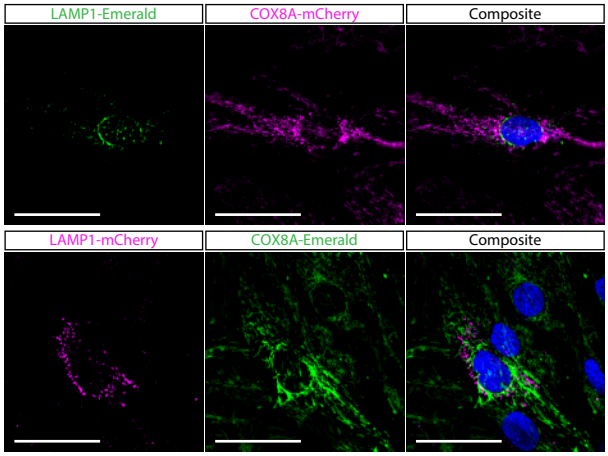

Figure 2

A.

B.

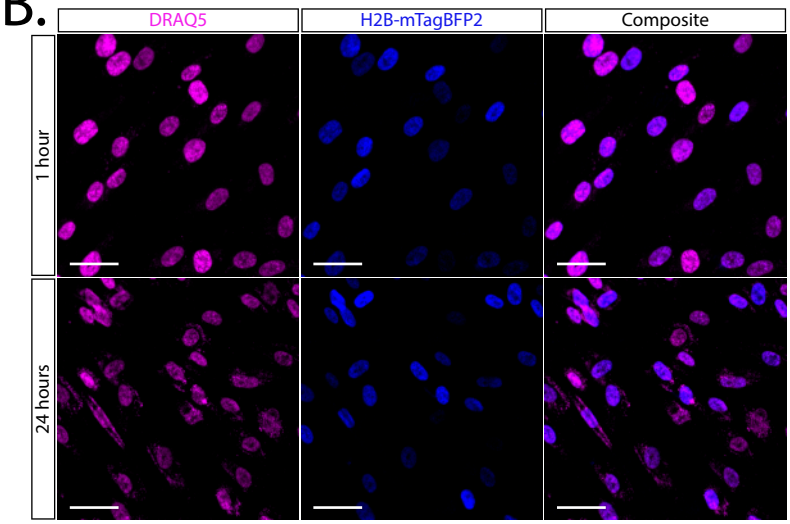

C.

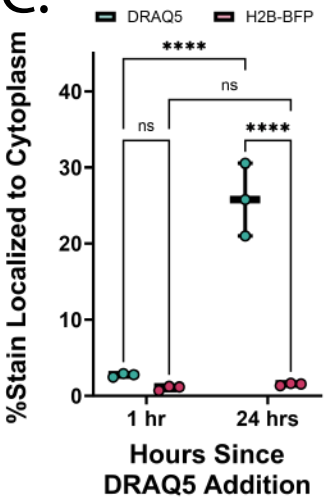

D.

E.

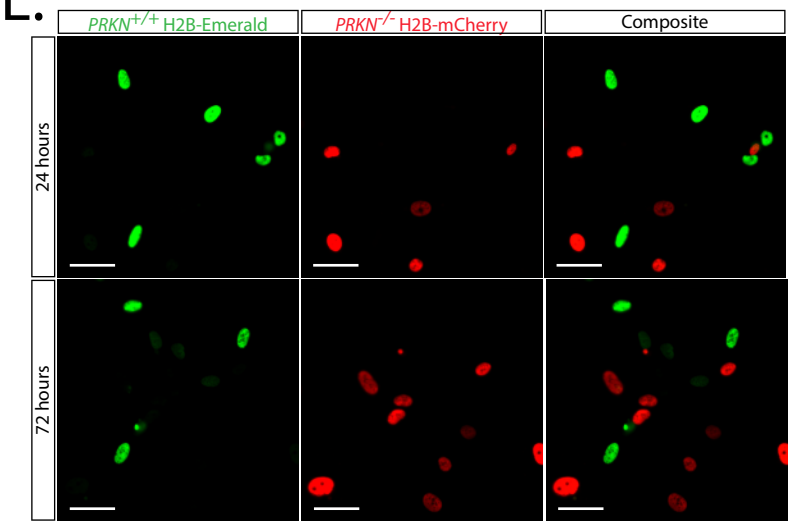

F.

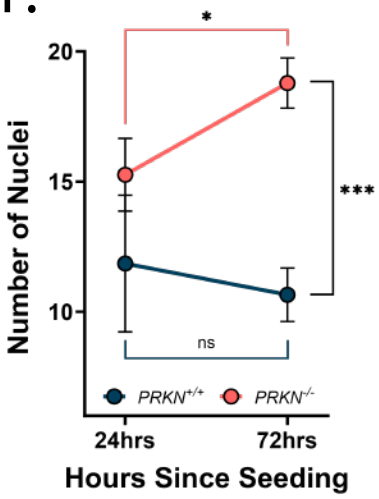

Figure 3

A.

B.

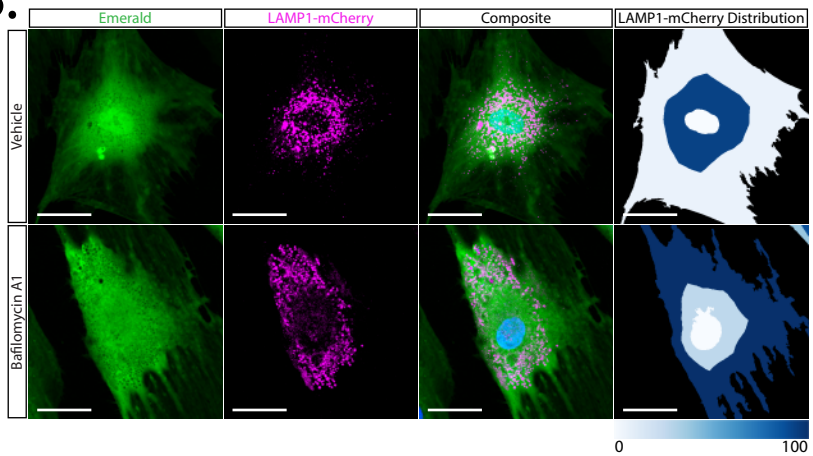

C.

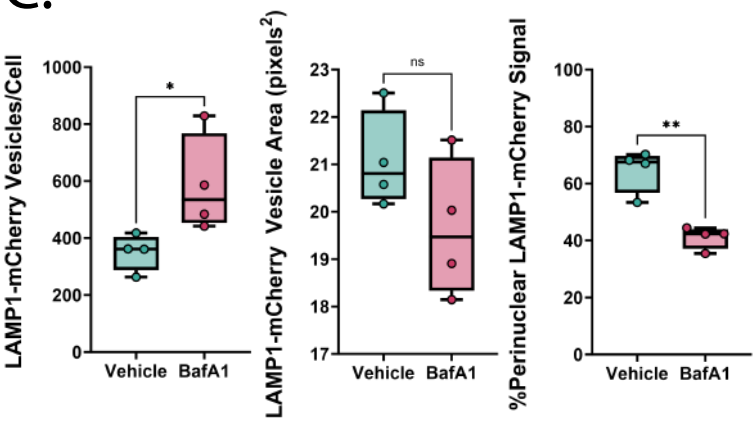

D.

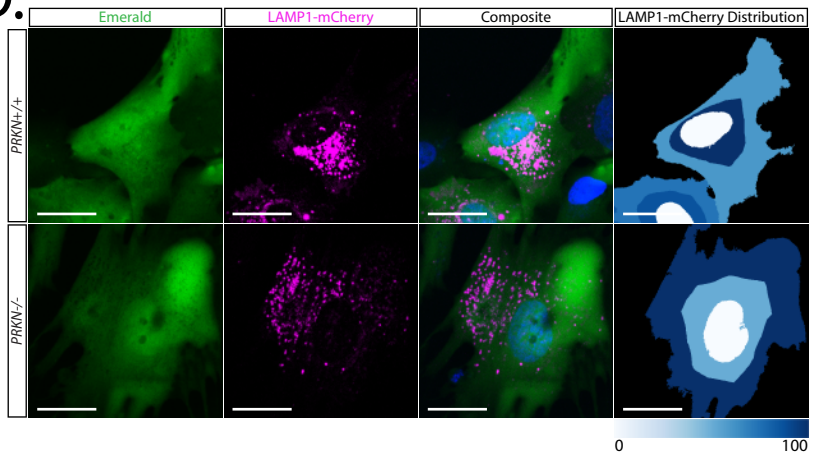

E.

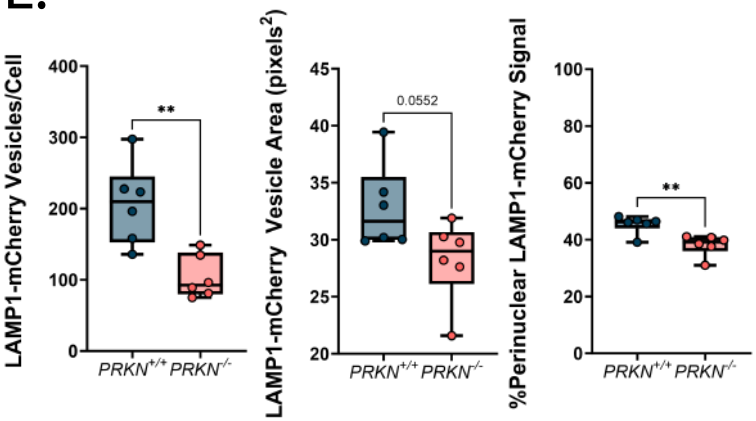

Figure 4

A.

B.

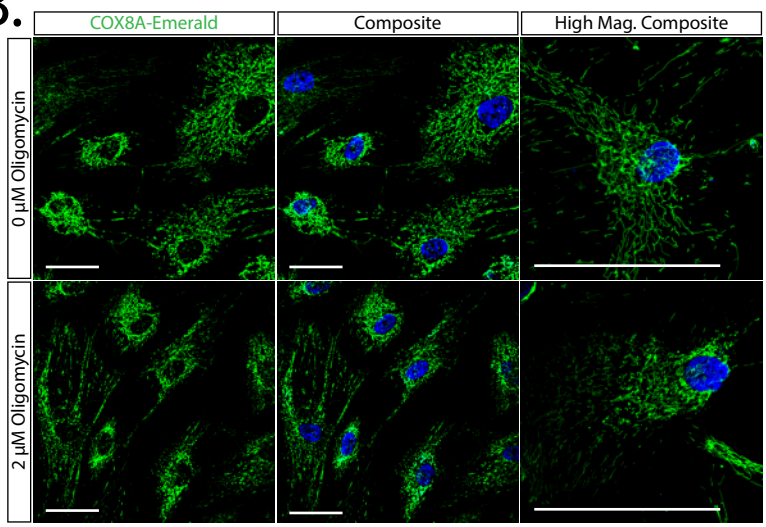

C.

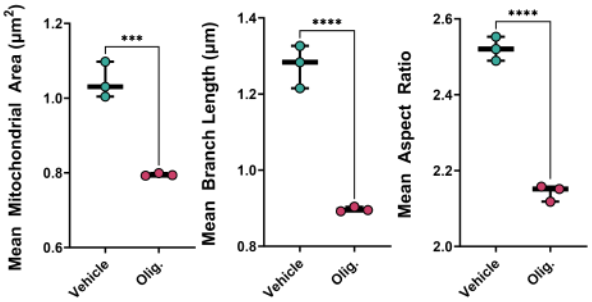

D.

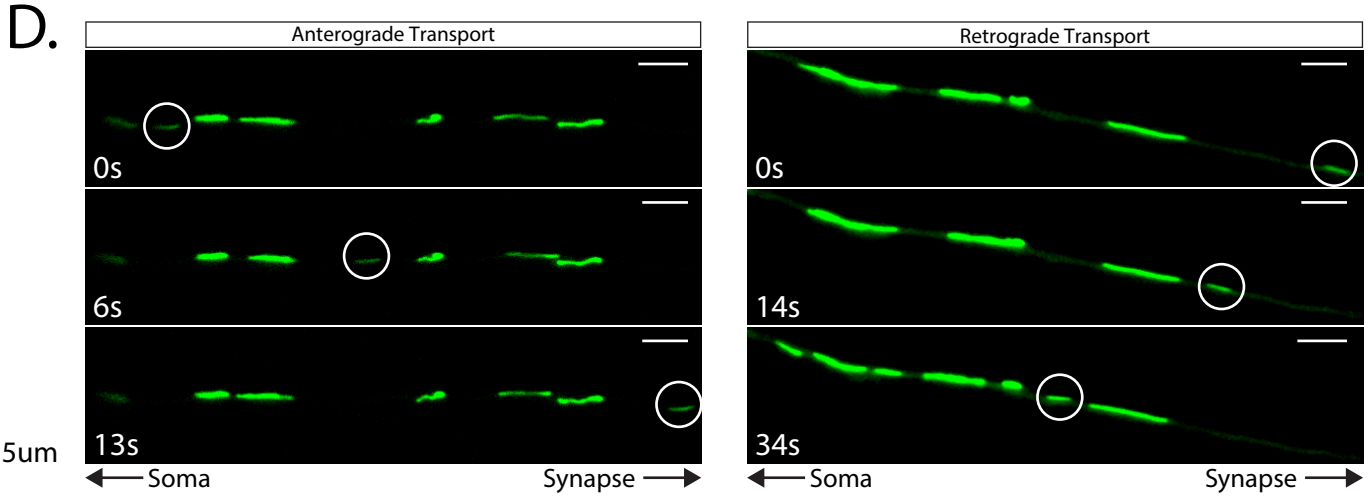

E.

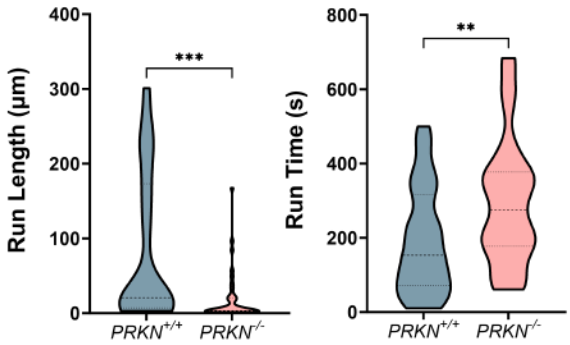

F.

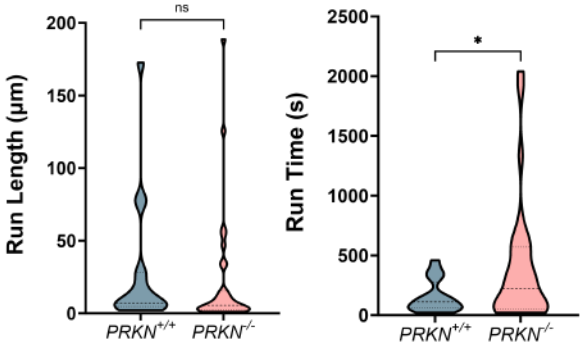

Figure 5

A.

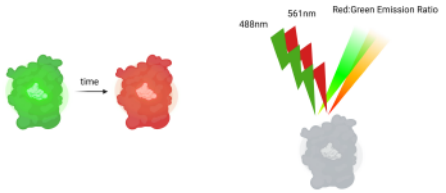

B.

C.

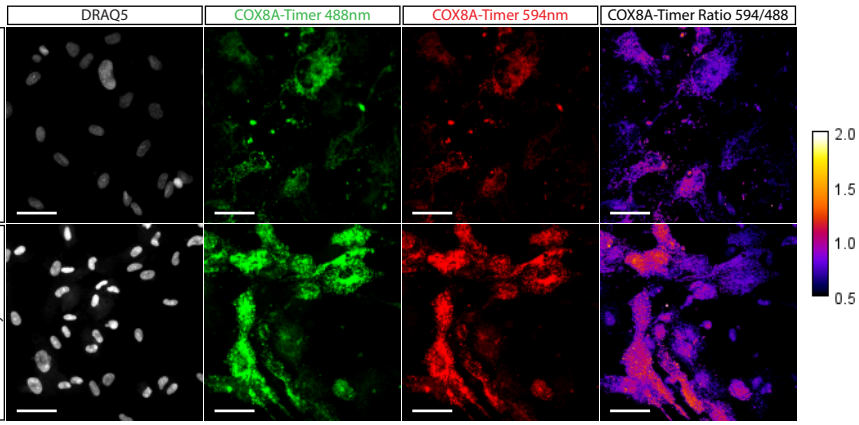

D.

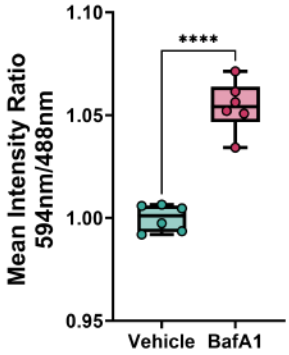

E.

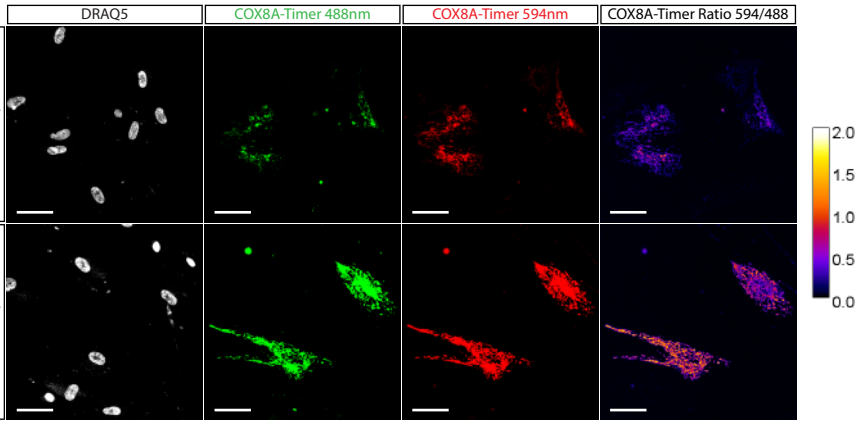

F.

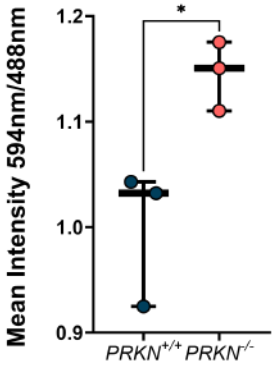

G.

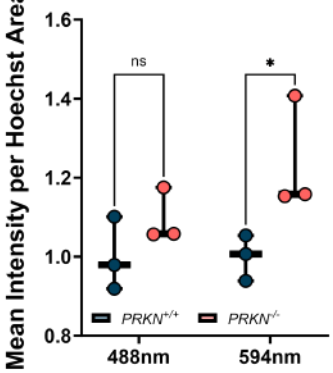

Figure 6

A.

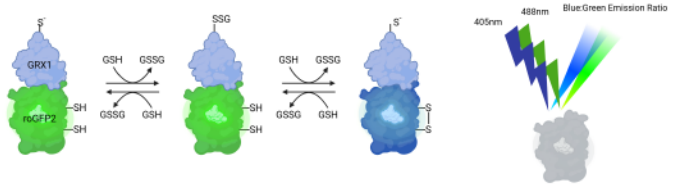

B.

C.

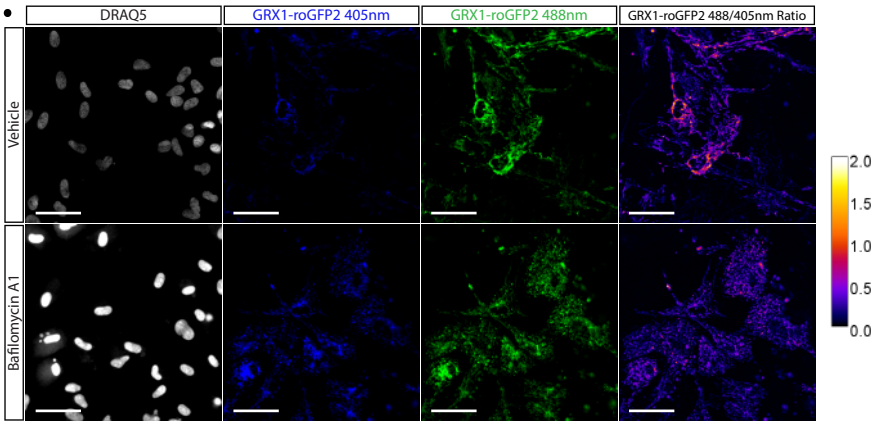

D.

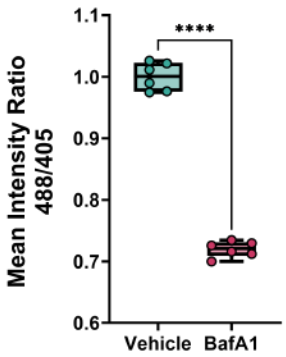

E.

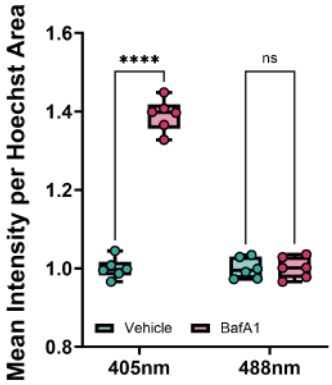

F.

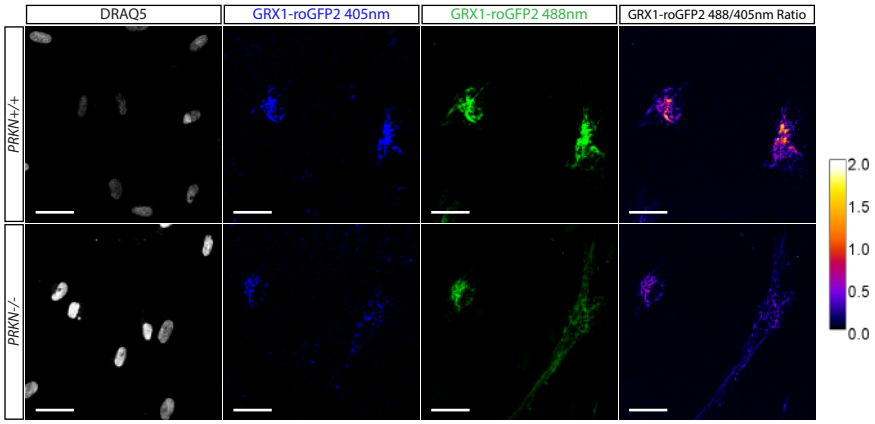

G.

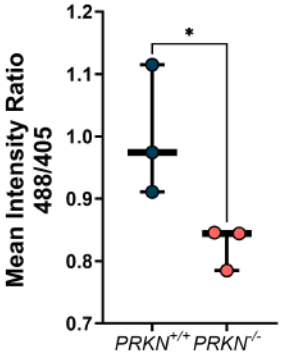

Figure S1

A.

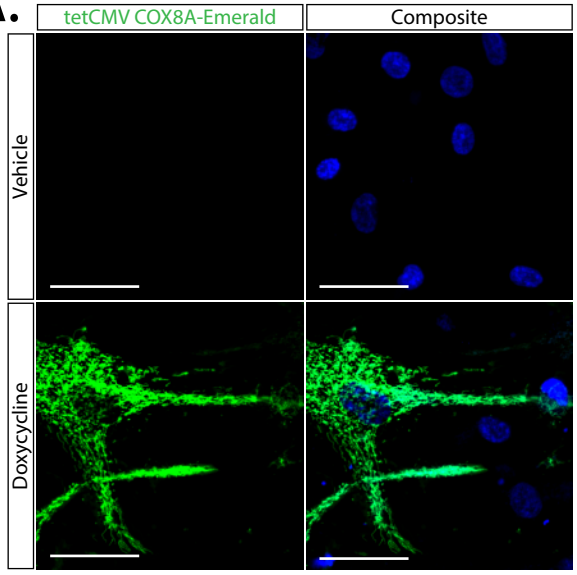

C.

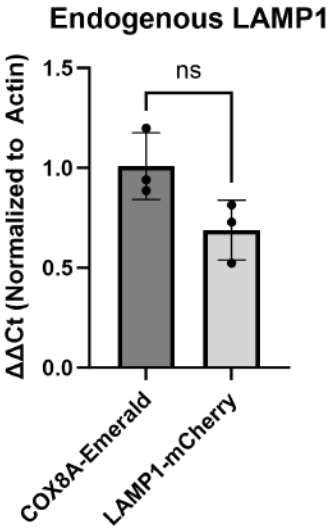

B.

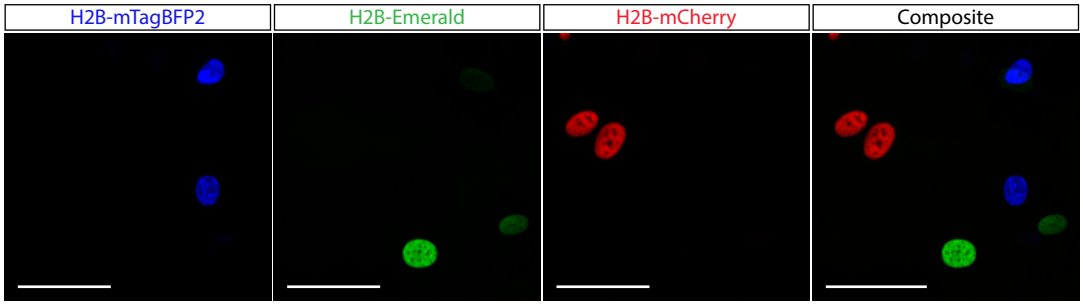

Figure S2

A.

UbC
Cox8A (Mitochondria)
Lemon
Empty (No Selection)

B.

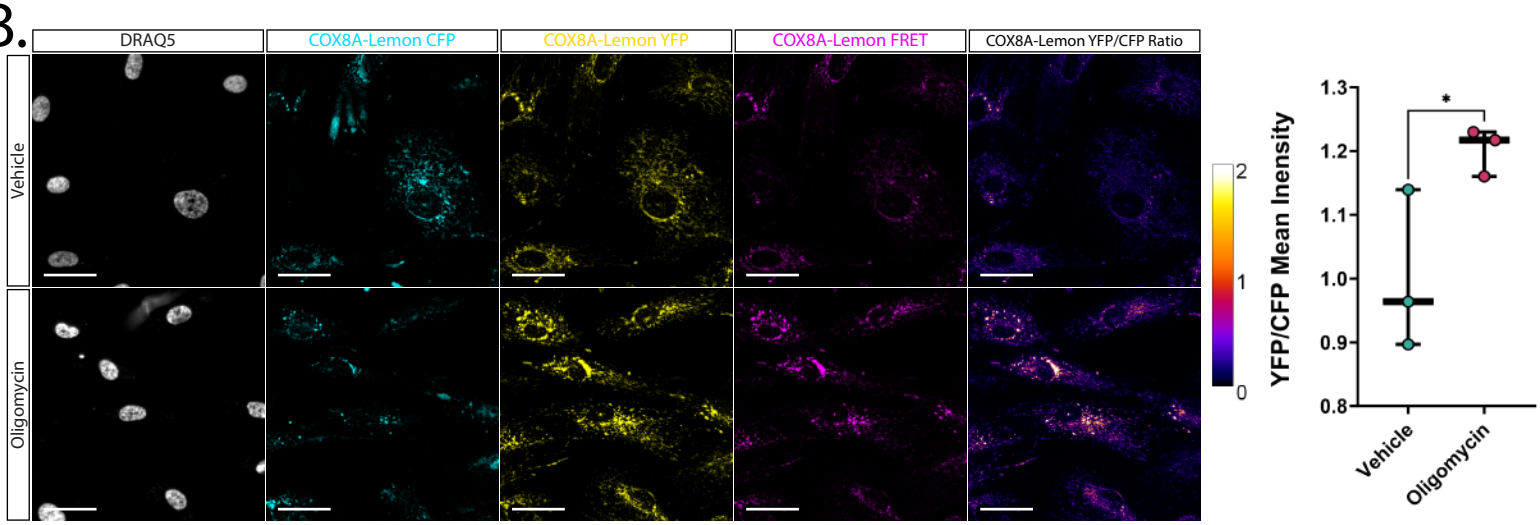
DRAQ5
COX8A-Lemon CFP
COX8A-Lemon YFP
COX8A-Lemon FRET
COX8A-Lemon YFP/CFP Ratio
Vehicle
Oligomycin
2
1
0
YFP/CFP Mean Inensity
1.3
1.2
1.1
1.0
0.9
0.8
*
Vehicle
Oligomycin

Figure S3

A.

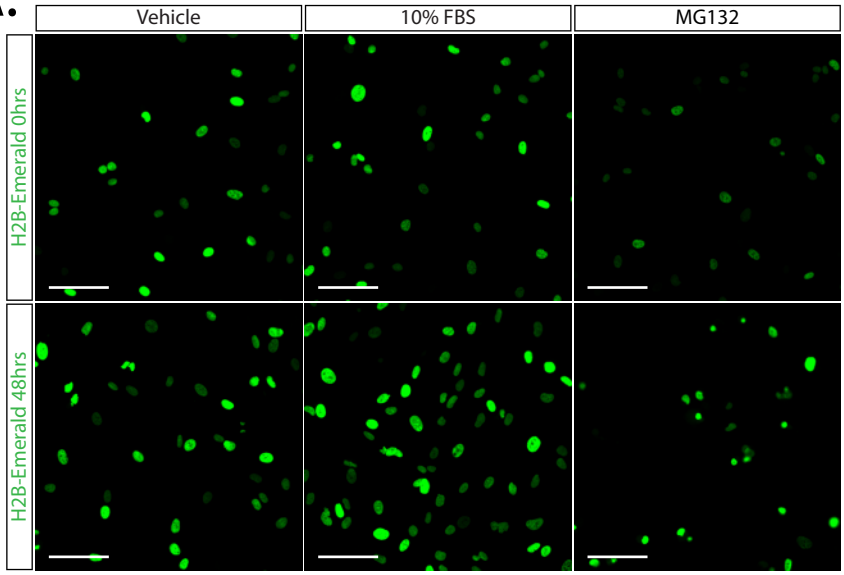
Vehicle
10% FBS
MG132
H2B-Emerald 0hrs
H2B-Emerald 48hrs

B.

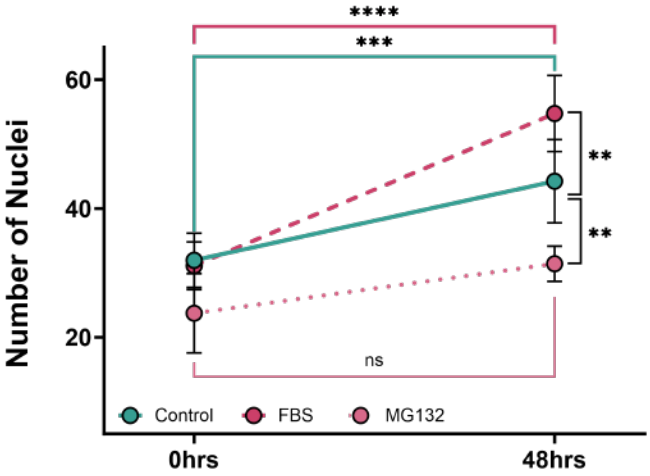
****
***
**
**
ns
Number of Nuclei
60
40
20
Control
FBS
MG132
0hrs
48hrs

Figure S4

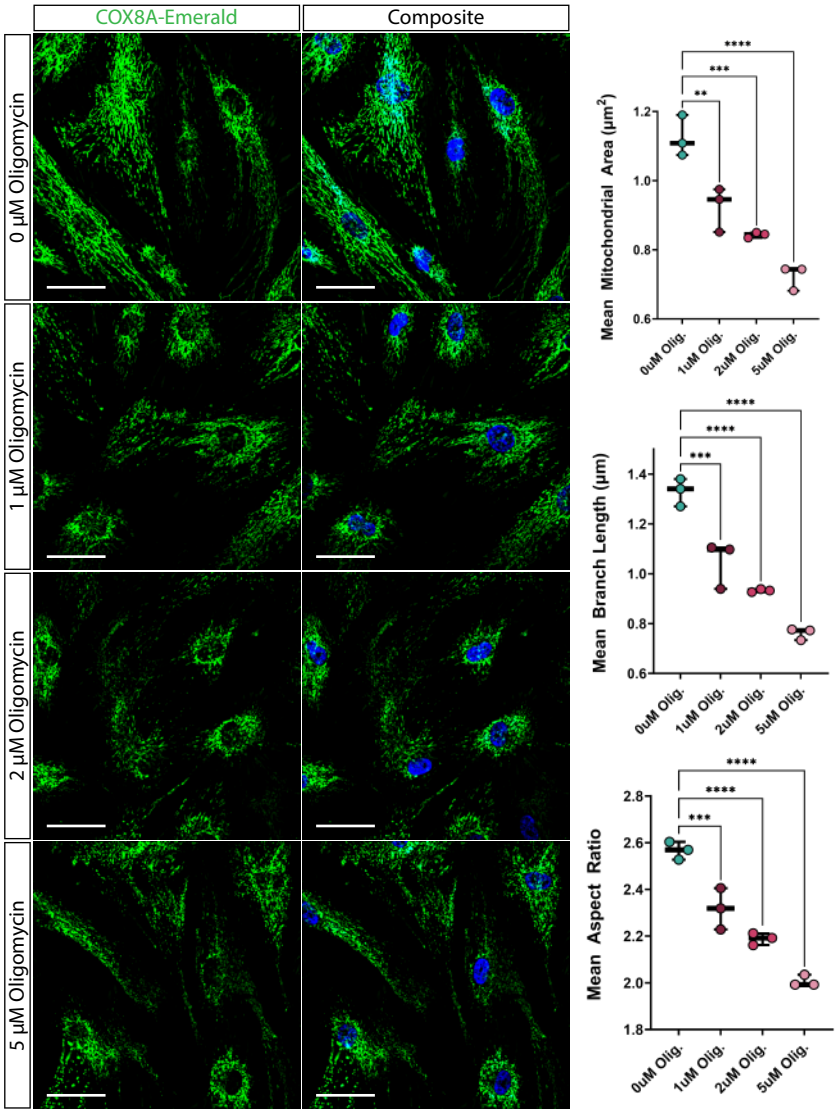
COX8A-Emerald
Composite
0 µM Oligomycin
1 µM Oligomycin
2 µM Oligomycin
5 µM Oligomycin
Mean Mitochondrial Area (µm²)
Mean Branch Length (µm)
Mean Aspect Ratio
0uM Olig.
1uM Olig.
2uM Olig.
5uM Olig.
****
***
**

Plasmid Name	Nickname	AddGene Cat#	Localization	Fluorophore	Antibiotic Resistance	Relevant Figure(s)
pFUW H2B-mTagBFP2-p2A-PuroR	H2B-mTagBFP2		Nucleus	mTagBFP2	Puromycin	1, 2, S1, S3
pFUW H2B-Emerald-p2A-PuroR	H2B-Emerald		Nucleus	Emerald	Puromycin	2, S1
pFUW H2B-mCherry-p2A-PuroR	H2B-mCherry		Nucleus	mCherry	Puromycin	2, S1
pFUW LAMP1Sig-Emerald	LAMP1-Emerald		Lysosome	Emerald	NA	1, 3
pFUW LAMP1Sig-mCherry	LAMP1-mCherry		Lysosome	mCherry	NA	1
pFUW COX8ASig-Emerald	COX8A-Emerald		Mitochondria	Emerald	NA	1, 4, S5
pFUW COX8ASig-mCherry	COX8A-mCherry		Mitochondria	mCherry	NA	1
pFUW PuroR-P2A-COX8ASig-Timer	COX8A-Timer		Mitochondria	Timer	Puromycin	5
pFUW COX8ASig-Lemon	COX8A-Lemon		Mitochondria	Lemon	NA	S2
pFUW mito-GRX1-roGFP2	mito-GRX1-roGFP2		Mitochondria	roGFP2	NA	6
pFUW mTagBFP2	mTagBFP2		NA	mTagBFP2	NA	NA
pFUW Emerald	Emerald		NA	Emerald	NA	NA
pFUW mCherry	mCherry		NA	mCherry	NA	NA
pFUW mTagBFP2-P2A-PuroR	mTagBFP2-PuroR		NA	mTagBFP2	Puromycin	NA
pFUW Emerald-P2A-PuroR	Emerald-PuroR		NA	Emerald	Puromycin	3
pFUW mCherry-P2A-PuroR	mCherry-PuroR		NA	mCherry	Puromycin	NA
pFUW mTagBFP2-P2A-NeoR	mTagBFP2-NeoR		NA	mTagBFP2	Neomycin	NA
pFUW Emerald-P2A-NeoR	Emerald-NeoR		NA	Emerald	Neomycin	NA
pFUW mCherry-P2A-NeoR	mCherry-NeoR		NA	mCherry	Neomycin	NA